Using Post-Processing Heat Treatments to Elucidate Precipitate Strengthening of Additively Manufactured Superalloy 718

Stephen Taller[1*], Ty Austin[2,3]

1 – Nuclear Energy and Fuel Cycle Division, Oak Ridge National Laboratory[†1]

2 – Manufacturing Sciences Division, Oak Ridge National Laboratory

3 – University of Tennessee, Knoxville

Abstract

The poor machinability and extensive work hardening of Ni-based superalloys makes additive manufacturing an attractive option for producing geometrically complex components with distinct microstructures. Although previous studies show recovery of high strength at room temperature, very few studies demonstrate successful properties at elevated temperatures required for industrial applications. The objectives of this study are to present a post-build heat treatment for high strength across a wide temperature range, determine the strength contribution of nanoscale precipitating phases to the overall mechanical properties of superalloy 718, and from these, provide a comprehensive microstructure-property relationship for wrought and AM 718 to guide efforts to simulate the properties of AM components. Laser powder bed fusion–produced superalloy 718 was characterized at multiple length scales using scanning electron microscopy and transmission electron microscopy in the as-built condition and with multiple heat treatments designed to form combinations of γ′, γ″, and δ precipitates. Uniaxial tensile tests performed from room temperature to 600 °C on subsize specimens determined the yield strength, elastic modulus, ultimate tensile strength, fracture stress, and uniform elongation. Precipitates in this work proved to be weak barriers to dislocation motion through a dispersed barrier model, but they provided strength to the alloy through their consistent high density. The relative contribution to the yield strength from γ″ remained consistent

*Corresponding Author: Stephen Taller, 1 Bethel Valley Rd., Oak Ridge, TN, 37830, TallerSA@ornl.gov

between 48–57% of the total strength up to 600 °C, the primary influence on the high temperature strength of superalloy 718. The strength factors for γ″ and δ precipitates were found to trend inversely with tensile test temperature and may be attributable to the differences in precipitate coherency. A post-build heat treatment is recommended to maintain high strength at elevated temperatures. A quantitative microstructure-property relationship, dependent on precipitate size, density, and morphology, was derived and can estimate the yield strength across a wide temperature range applicable to the operational regimes for superalloy 718.

Key words: Alloy 718, heat treatment, precipitation, tensile properties, laser powder bed fusion

1. Introduction

Ni-based superalloys are a primary candidate alloy class for high-temperature applications in the petrochemical, aerospace, and nuclear power industries because of their intrinsic resistance to creep, their adequate corrosion resistance, and the ability to tailor the microstructure for high strength [1,2]. These high-strength Ni-based alloys gain their strength primarily through solid solution strengthening and/or secondary precipitating phases in the lattice [3], such as the intermetallic phases δ, γ′, or γ″. The poor machinability and extensive work hardening of Ni-based superalloys makes additive manufacturing (AM) an attractive option to produce geometrically complex components. Powder bed fusion – laser beam (PBF-LB) is an AM process used to build parts through sequential application of thin layers (20–100 μm) of metal feedstock powder melted by a scanning laser, resulting in rapid solidification and thermal cycling, and has been used to produce parts from a Ni-based superalloy, 718 [4–6].

Despite the continual improvement in processing parameters, the microstructures of AM materials typically contain a high density of pores and other nonequilibrium features that encourage the use of post-fabrication heat treatments [5]. Like alloy 718, many nickel superalloys have compositions that allow for the formation of many different precipitating phases, all of which may result from PBF-LB. Several of these appear to be beneficial for the alloy at high temperatures (γ′ and γ″), whereas alternative phases (δ and Laves) are detrimental [7,8]. Post-build heat treatments typically include direct aging, solution annealing, hot isostatic pressing (HIP), or a combination [9–13] in an attempt to produce a high strength component

[14]. The literature of post-build heat treatments show varying degrees of success [6,15,16] to achieve a yield strength in the range of 800 - 1300 MPa at room temperature but with visible δ and Laves particles [17]. In many cases, an additional step of a high temperature homogenization at 1100 °C or greater was needed to result in high strength [18,19] and does not always eliminate the Laves phase [20–22] or porosity [23]. For a comprehensive review, the reader is referred to a recent article [24] on laser bed fusion of Ni-based superalloys highlighting many of the processing parameter studies, heat treatments, and properties from which this study was pursued, and the challenges with unpredictable heat treatments for precipitation hardening. Although high strength can be recovered at room temperature, very few studies demonstrate success over the wide operating temperature regime from room temperature to 650 °C for superalloy 718. There is still a need to determine a post-processing heat treatment of additively manufactured superalloy 718 that results in high strength at the elevated temperatures expected during service and eliminates detrimental phases.

Furthermore, as the strength of the 3D-printed component depends on the nanoscale particles that develop during the repetitive heating and cooling cycles associated with AM, there is a significant need to understand how each precipitate that can be formed from AM contributes to the overall strength of the alloy. The objectives of this study are 1) to demonstrate the combination of a two-step post-build high temperature normalization and aging heat treatments on the microstructure and mechanical properties of alloy 718, and 2) use the post-heat treatment properties to determine the strength contribution of nanoscale precipitating phases to the overall mechanical properties of Superalloy 718 through a combination of electron microscopy and uniaxial tensile straining. The results of this study will be used to recommend a post-build heat treatment and provide a physically informed equation connecting the microstructure and yield strength across elevated temperatures for modeling and simulation. Superalloy 718 was characterized in the as-built condition, and with multiple heat treatments, to form δ precipitates, as well as γ′ and γ″ precipitates at multiple length scales using scanning electron microscopy (SEM) and transmission electron microscopy (TEM) to correlate the microstructure to the bulk properties. Uniaxial tensile tests were performed under conditions ranging from room temperature to 600 °C on subsize specimens to determine

the common engineering properties of yield strength, elastic modulus, ultimate tensile strength, uniform elongation, and total elongation. An Orowan dispersed barrier hardening model was used to assess the contributions of microstructural features to the yield strength as a function of tensile test temperatures, and from the calculated trends, to elucidate the role of precipitate coherency on tensile strength. The microstructure-property relationship derived from this work can be used to estimate the yield strength of wrought and AM superalloy 718 components across a wide temperature range applicable to the operational regimes for nickel superalloys.

2. Methodology

2.1 Composition, Fabrication and Heat Treatments

The additively manufactured superalloy 718, designated AM718, used in this investigation was printed in one build cycle by using PBF-LB on the Concept X-Line 2000R at the Manufacturing Demonstration Facility (MDF) at Oak Ridge National Laboratory (ORNL, build ID: 20200206XL) using a powder with the composition listed in Table 1 with process parameters of a laser power of 370 W, spot size of 300 μm, scanning speed of 500 mm/s, and hatch spacing of 0.16 mm with 67° rotation between layers. The plate was sectioned into four pieces: three for subsequent heat treatments, and one for the as-built (ASB) microstructure. Three heat treatments, summarized in Table 2 and shown schematically in Figure 1 with the time-temperature-transformation (TTT) diagram for superalloy 718, were designed to reduce the complexity of the AM microstructure and to allow for comparative analysis of the microstructure and mechanical properties. Based on the work performed by Poole et al. [25] to identify the δ and Laves phase solvus temperatures, a two-step homogenization treatment of 1,174 °C for 2 h followed by 1,204 °C for 6 h was chosen to remove all secondary phases, including the detrimental Laves phase that typically forms during AM and competes with δ, γ′, and γ″ precipitates for Nb [14]. Annealing further at 1,093 °C for 1 h with no additional heat treatments provides a reference case solution-annealed alloy 718 with minimal precipitation, designated as AM718-HM. The extensive knowledge of the precipitation in alloy 718 [26–30] led to the adoption of a standard heat treatment to produce δ precipitates that consists of solution annealing at 945 °C followed by aging at 718 °C and then 621 °C for 8 hours at each step, shortened to 945 °C/718 °C/621 °C

[30–32], and designated as AM718-HT1. A higher temperature heat treatment of 1,093 °C/718 °C/621 °C was chosen to form a large density of small γ′ and γ″ precipitates based on the work performed in [8,30,31], designated as AM718-HT2. A traditional wrought alloy 718, designated W718 heat Z1653 was prepared according to ASTM specifications [33], was used as a control, and was compared with the AM specimens. However, as demonstrated further in the article, the same heat treatment for AM718-HT2 and W718 resulted in distinct microstructures and mechanical properties. and the reader is referred to the Appendix for more details. After heat treatment, specimens were fabricated into the form of SS-J2 subsize tensile specimens [34], displayed in Figure 2, for uniaxial tensile tests with a gauge 5 mm long, 0.5 mm thick, and 1.2 mm wide using electrical discharge machining (EDM). The SS-J2 geometry was chosen to minimize the amount of material needed for testing, provide adequate tensile property measurements [35], and allow for future studies in which subsize specimens will be used. Each specimen was individually engraved via a laser with a unique ID for tracking from the original build plate to the tensile specimen. Previously obtained results for room temperature properties and preliminary characterization were reported by Taller et al. [36], from which this manuscript builds.

Table 1. Composition of superalloy 718 powder used for PBF-LB in wt % provided by the vendor for Lot 119 and a commercially purchased wrought superalloy 718 for comparison as measured with x-ray fluorescence.

Designation	Ni	Fe	Cr	Nb	Mo	Ti	Al	Si	C	N	O	Co	B	Mn	P	S
AM718-Lot 119	Bal.	18.22	18.99	5.15	3.0	0.93	0.50	0.04	0.04	0.012	0.016	0.1	0.001	0.02	0.006	0.001
W718-Z1653	Bal.	18.77	17.56	5.18	2.89	0.94	0.49	0.08	0.02	-	-	0.05	0.004	0.03	0.008	<0.0003
ASTM-B670 Reference [37]	50.0 – 55.0	Bal.	17.0 – 21.0	4.75 – 5.50	2.8 – 3.3	0.65 – 1.15	0.2 – 0.8	0.35 max	0.08 max	-	-	1.0 max	0.006 max	0.35 max	0.015 max	0.015 max

Table 2. Heat treatments for AM718 and W718 to produce increasingly simpler microstructures for characterization and mechanical property measurement. The cooling between steps was performed using either water cooling (WC) or air cooling (AC).

Designation	Homogenization (°C/h)	Cooling	Solution anneal (°C/h)	Cooling	Aging #1 (°C/h)	Cooling rate to reach aging #2 (°C/h)	Aging #2 (°C/h)	Cooling rate to room temp.
W718-Z1653	1174/2+1204/6	WC	1093/1	AC	718/8	55	621/8	AC
AM718-HT1	1174/2+1204/6	WC	945/1	AC	718/8	55	621/8	AC
AM718-HT2	1174/2+1204/6	WC	1093/1	AC	718/8	55	621/8	AC
AM718-HM	1174/2+1204/6	WC	1093/1	AC	N/A	N/A	N/A	N/A

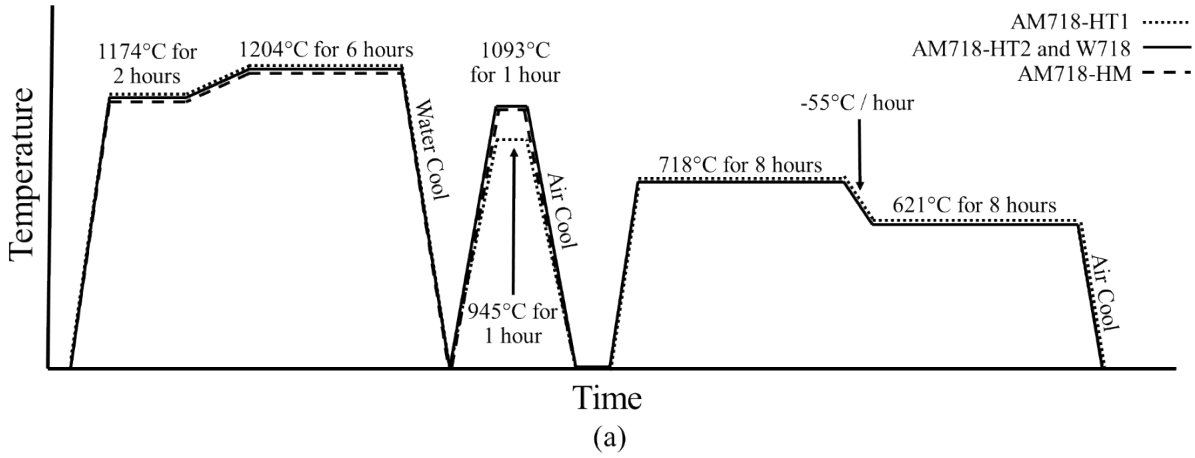

(a)

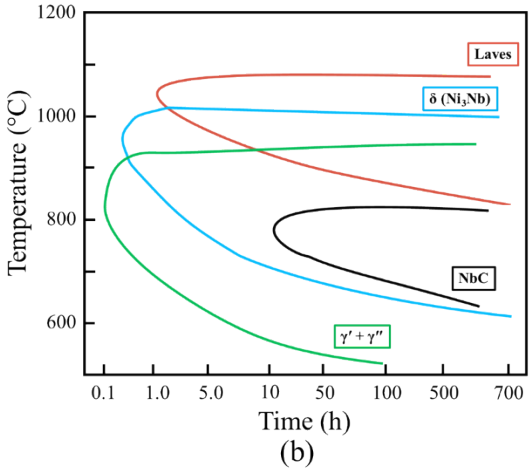

(b)

Figure 1. The (a) time-temperature diagram for the heat treatments in this study with (b) a TTT diagram for alloy 718 derived from [8,38,39]**.**

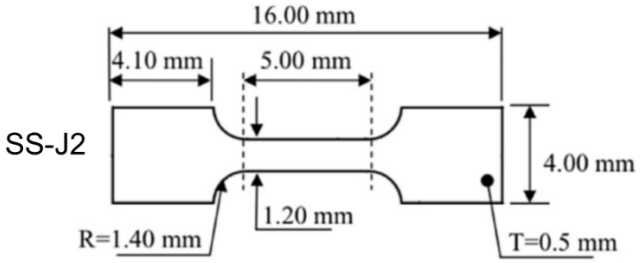

Figure 2. Schematic of the subsize tensile specimens with appropriate dimensions.

2.2 Microscopy

Prior to characterization, standard metallographic grinding using successively finer grits of SiC paper and polishing using diamond solutions with successively decreasing particle sizes of 6 μm, 3 μm, and 0.25 μm were performed until a mirror-like surface was achieved with ~0.02 μm silica particles. Surface characterization was performed on a Tescan MIRA3 GHM scanning electron microscope (SEM) using 20 keV electrons. Electron backscatter diffraction (EBSD) Kikuchi band patterns were collected on an Oxford Instruments Symmetry EBSD detector with AZtec software using a step size of 1 μm. At each point, the AZtec software indexes the Kikuchi band structure and determines the Euler angles of the lattice. The open source MTEX toolbox [40] was used to generate orientation maps and inverse pole figures and to determine grain sizes from the Euler angles exported from AZtec for grains consisting of more than 5 pixels. The equivalent grain diameter was calculated by taking the area of the grain determined by the orientation map and assuming a circular area through Eq. (1):

$$d_{eq} = 2\sqrt{\frac{A}{\pi}}. \quad (1)$$

TEM lamellae were prepared on an FEI Versa™ Nanolab™ 650 or an FEI Quanta™ Nanolab™ focused ion beam (FIB) system by using standardized lift-out procedures. Each lamella was made with a

thick window frame to minimize foil bending and twisting during sample thinning below a thickness of ~300 nm. Low-energy Ga ion beams at 2 and 5 keV were used to thin the ~150 nm thick lamella to a final thickness of around 80–100 nm, which effectively eliminated the TEM-visible FIB damage induced at high-beam energy. For each condition, two lamellae were extracted from different grains comprising of at least 25 μm^2 of electron transparent area to assess uniformity.

The nanoscale microstructure for each heat treatment of AM718 and W718 was characterized by using the FEI Talos F200X scanning transmission electron microscope (STEM) instrument equipped with high counting rate electron dispersive spectroscopy (EDS). Before imaging and EDS spectra collection, the lamella was tilted to a low-order zone axis such as the (001), and the collection angles were optimized. Each STEM image set consisting of Bright Field (BF), Dark Field (DF), and High Angle Annular Dark Field (HAADF) images was collected with a region of interest size of 2,048 × 2,048 pixels with a resolution of ~0.7 nm/pixel. Additional images were collected as needed at a higher resolution of 0.16 nm/pixel to confirm the precipitate structure and composition. EDS-based spectrum images for precipitate measurement were taken over a broad area by using a region-of-interest size of 1,024 × 1,024 pixels with a resolution of ~1.3 nm/pixel, a probe full-width half-maximum of ~1.5 nm, and a beam current of around 3 nA. Each scan had a duration of 1 h, with more than 35,000 counts/s and dead times from 1–6%. The qualitative x-ray counts were converted to quantified weight percentages by using the Cliff-Lorimer [41] method for calculation at each pixel.

Each corresponding collection of STEM images and EDS spectrum images was characterized for nanoscale features. Precipitates were identified by using the composition expected for each phase [38] and overlaying the corresponding EDS maps for the elements of interest in the phase. Phase identification was assisted using a trained dynamic segmentation convolutional neural network [42]. Each feature was annotated by the neural network and designated as belonging to a class. These annotations were used to produce an image in which the type of feature present at any given pixel was labeled by a class number. Each feature class was individually filtered out of the image and analyzed by using the particle analysis function in FIJI [43] to obtain parameters for the area, perimeter, minimum width, maximum width, and

circularity for each feature present. When features were found to overlap in the two-dimensional image, the features were separated manually and confirmed using hand counting procedures. An equivalent diameter for each feature to use with the dispersed barrier hardening model was calculated using Eq. (2). The mean and standard error of the mean for the equivalent diameter were calculated for each identified feature of the microstructure.

$$d_{eq} = \sqrt{major\ axis \times minor\ axis}. \quad (2)$$

2.3 Uniaxial Tensile Testing

Subsize SS-J2 specimens were tested for common engineering properties by using uniaxial tensile straining. Five specimens of each heat treatment of the AM718 and W718 were strained at room temperature, 300 °C, 450 °C, or 600 °C. Tensile straining was conducted according to ASTM E8/E8M for room temperature and ASTM E21-20 for elevated temperatures on an MTS Systems uniaxial test frame. The straining was maintained at a crosshead displacement of 0.15 mm/min for a strain rate of 5×10^{-4} s^{-1} to avoid complications typical at high strain rates [44]. Specimens were strained to failure at the test temperature.

3. Results

3.1 Grain size determination

Representative forescatter SEM images and corresponding colorized EBSD orientation maps are shown in Figure 3. The wrought alloy 718 displayed the expected microstructure consisting of large grains with an average equivalent grain diameter of 106 ± 21.8 μm gathered from three areas containing 229 grains and with interior annealing twins. For AM718, the as-built microstructure consisted of elongated grains that showed a preferred orientation along the build direction, resulting in an average equivalent grain diameter of 8.3 ± 0.22 μm from 10 areas containing 3732 grains. The grain size distributions normalized by the total number of grains observed for the AM718 in the as-built and heat-treated conditions are shown in Figure 4. With the application of the homogenization heat treatment and subsequent solution anneal, incomplete

196 recrystallization occurred, leading to a mixture of large and small grains in the heat-treated AM conditions
197 and average equivalent grain diameters of 24.6. ± 2.5 μm gathered from three areas containing 342 grains
198 for AM718-HT1, 29.4. ± 2.8 μm gathered from three areas containing 315 grains for AM718-HT2, and
199 37.9. ± 2.6 μm gathered from three areas containing 442 grains for AM718-HM. However, the skewness
200 of the distributions may make the median a more relevant parameter which results in median equivalent
201 diameters of 3.1, 9.9, 12.5, and 18.8 μm for AM718-ASB, AM718-HT1, AM718-HT2, and AM718-HM,
202 respectively, and 62.7 μm for W718. With each heat treatment, the tail of the grain size distributions
203 extended to larger sizes, but the subsequent aging steps did not significantly increase the grain size further.

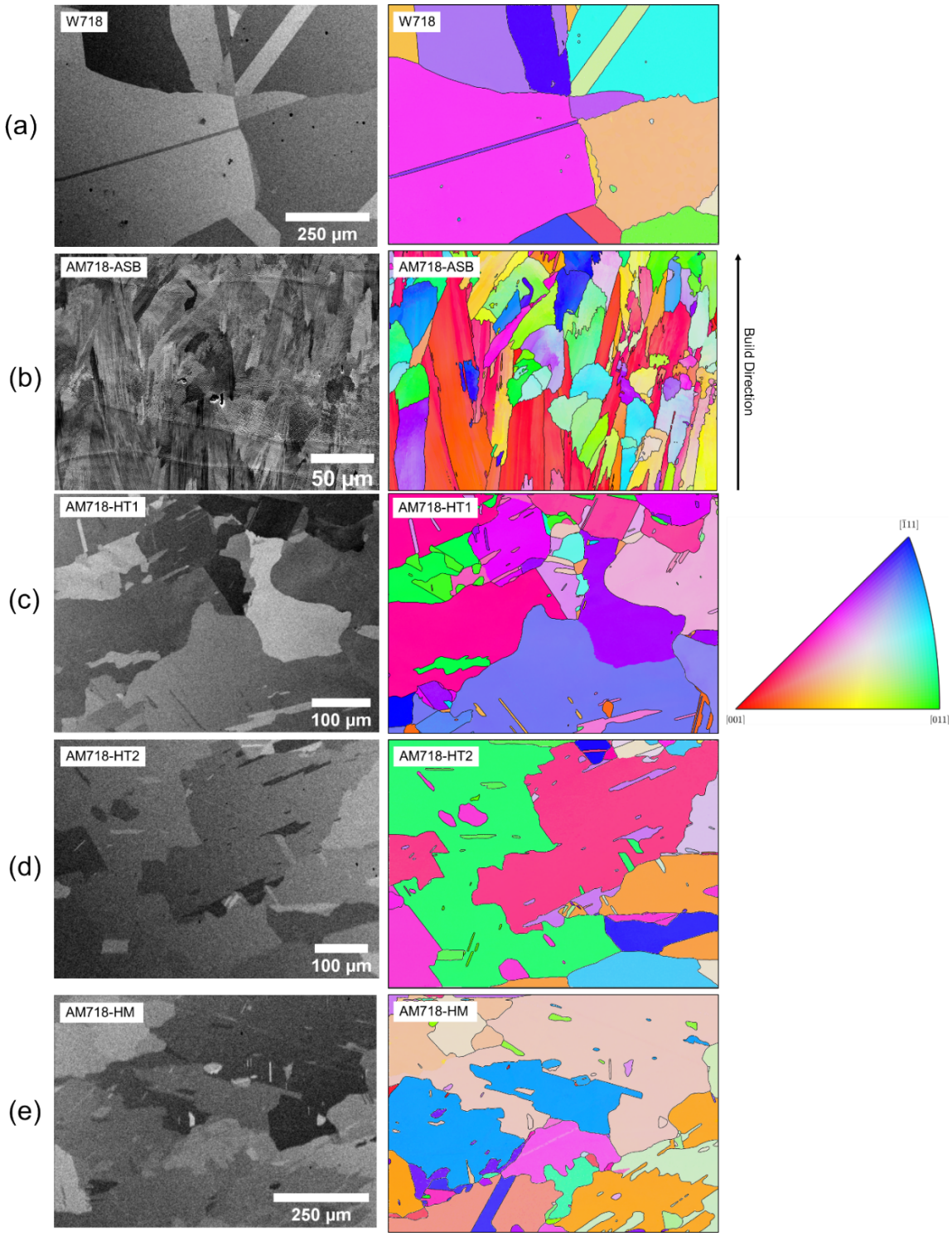

Figure 3. Representative forescatter electron images and corresponding EBSD orientation maps for (a) W718, (b) AM718-ASB, (c) AM718-HT1, (d) AM718-HT2, and (e) AM718-HM.

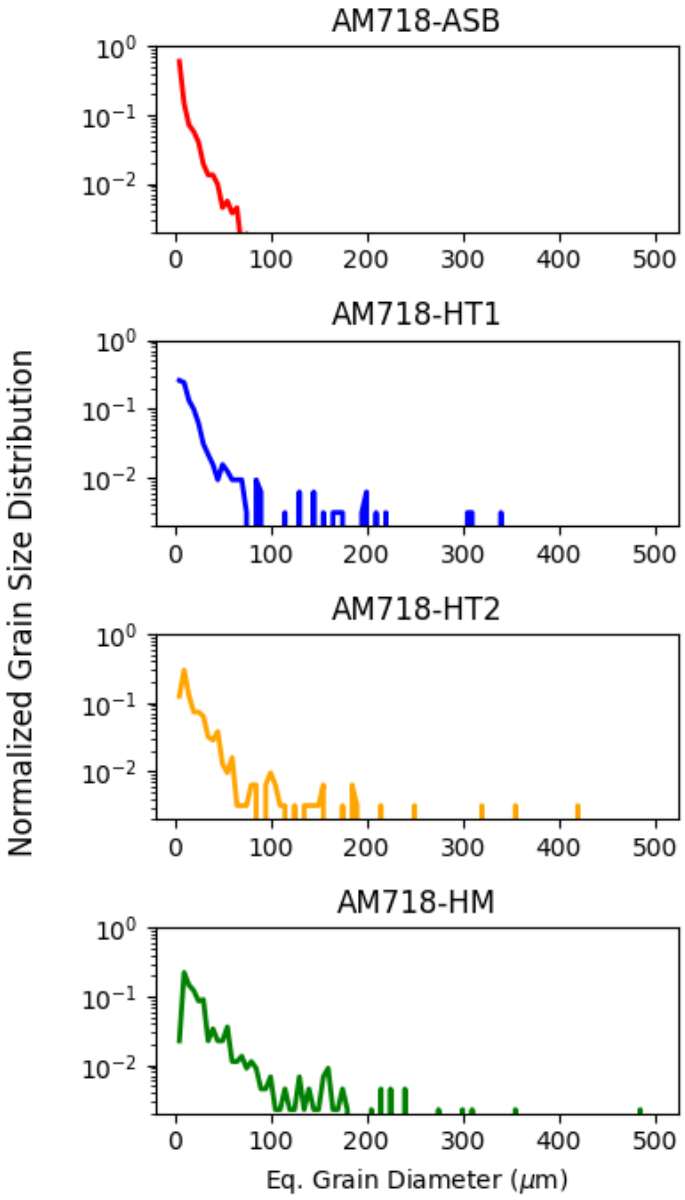

208

209 **Figure 4. Grain size distributions for AM718 normalized by the total number of grains captured within the EBSD map**
210 **areas.**

211

212 3.2 Precipitate Characterization Using STEM

213 The first characterization performed was on the ASB superalloy 718. An overview of the
214 microstructure at the micron scale is shown in Figure 5, in which the print direction is out of the page. The
215 grain structure consisted of fine lath-like boundaries decorated with Nb-rich precipitates. Toward the part

exterior, the Laves phase formed as a dendrite, and the δ phase formed on boundaries nearer to the part's interior. For volumes of the part consistently above the δ solvus line at 1,010 °C [45,46], Laves phase formation is preferred as a metastable phase from solidification at high cooling rates, whereas the δ phase forms latter in the fabrication process, likely from the longer time at elevated temperatures, to form the stable phase. At a higher magnification, a high density of γ″ precipitates was observed in the vicinity of larger δ phase particles (Figure 6), which is consistent with previous observations from AM-fabricated superalloy 718 [47] and as-cast wrought alloy 718 [46]. The time-temperature-precipitation diagram suggests that at higher temperatures such as those present during AM, the formation of interdendritic γ″ was favored over γ″ interior to the grain [47]. Interspersed throughout the grain interiors was a mixture of fine γ′ and γ″ precipitates of a very high density (Figure 7) with the frequency size distributions in Figure 8. Two nonoverlapping areas were examined for precipitate formation closer to the part interior to attempt to capture representative microstructures and determine the local heterogeneity in the microstructure. A quantitative summary of the observed microstructure is included in Table 3, including the number of precipitates observed, the percentage that each precipitate phase contributes to the total precipitation, the mean equivalent diameter, the standard error of the mean equivalent diameter, and the number density for each phase. Between the two areas examined, the size and density of γ″, Laves, and oxide precipitates were found to be nearly identical. However, both γ′ and δ showed a large variation in density (~2×) between ASB-1 and ASB-2, with no carbides being observed in ASB-2. Although mechanical properties could be obtained for comparison with this microstructure, it is unlikely to yield correlative results because of the high level of complexity and heterogeneity found in the ASB superalloy 718. Therefore, ASB superalloy 718 was excluded from the mechanical testing campaign and is not included in subsequent sections.

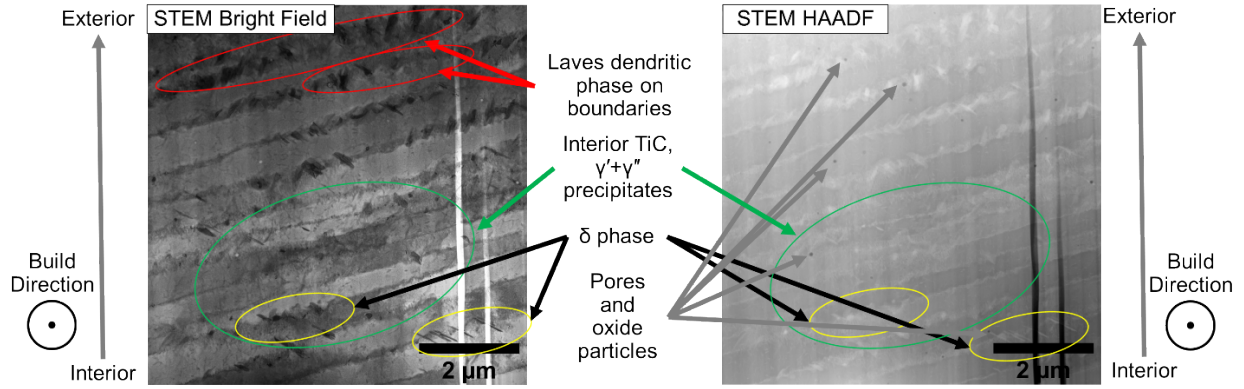

Figure 5. STEM images of ASB AM Superalloy 718 showing dendritic Laves phase, large δ precipitates, TiC, pores, oxide particles, and γ′ and γ″ precipitates as a function of distance from the part surface. Note the build direction vector is directed out of the page towards the viewer.

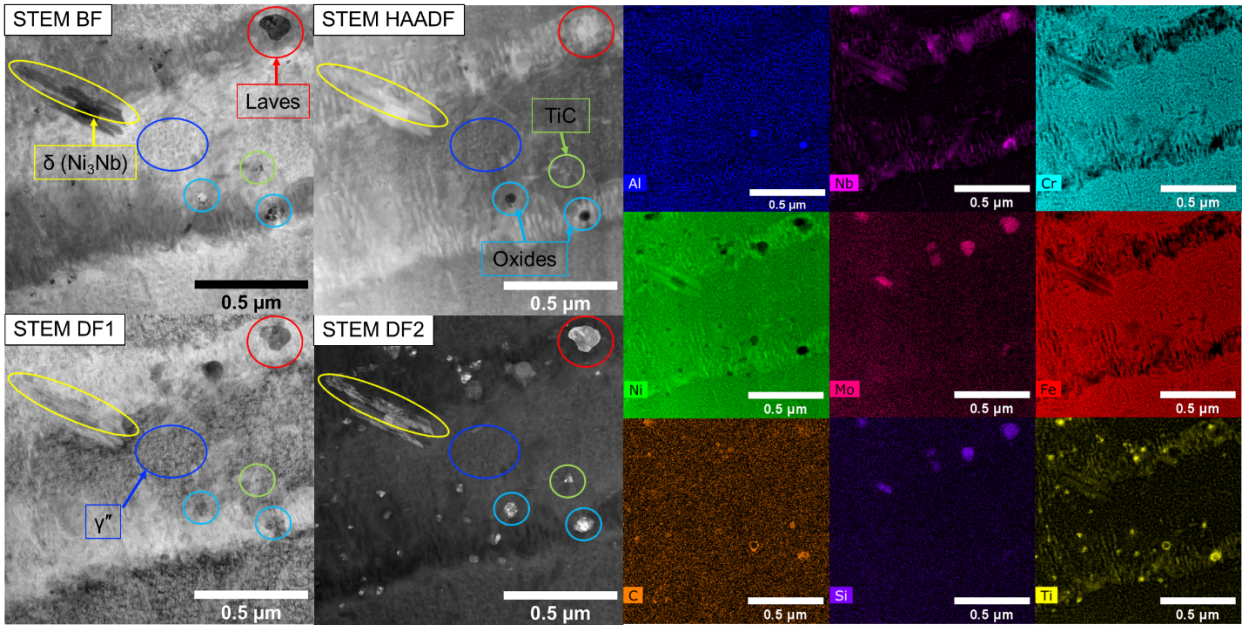

Figure 6. STEM images of ASB AM Superalloy 718 with corresponding EDS maps for precipitate-forming elements showing large δ precipitates circled in yellow (Ni_3Nb), Laves particles circled in red(Nb-Mo-Si rich), TiC, and γ″ precipitates circled in blue (Ni_3Nb), and oxide particles circled in light blue. For interpretation of the references to color in this figure, the reader is referred to the web version of this article.

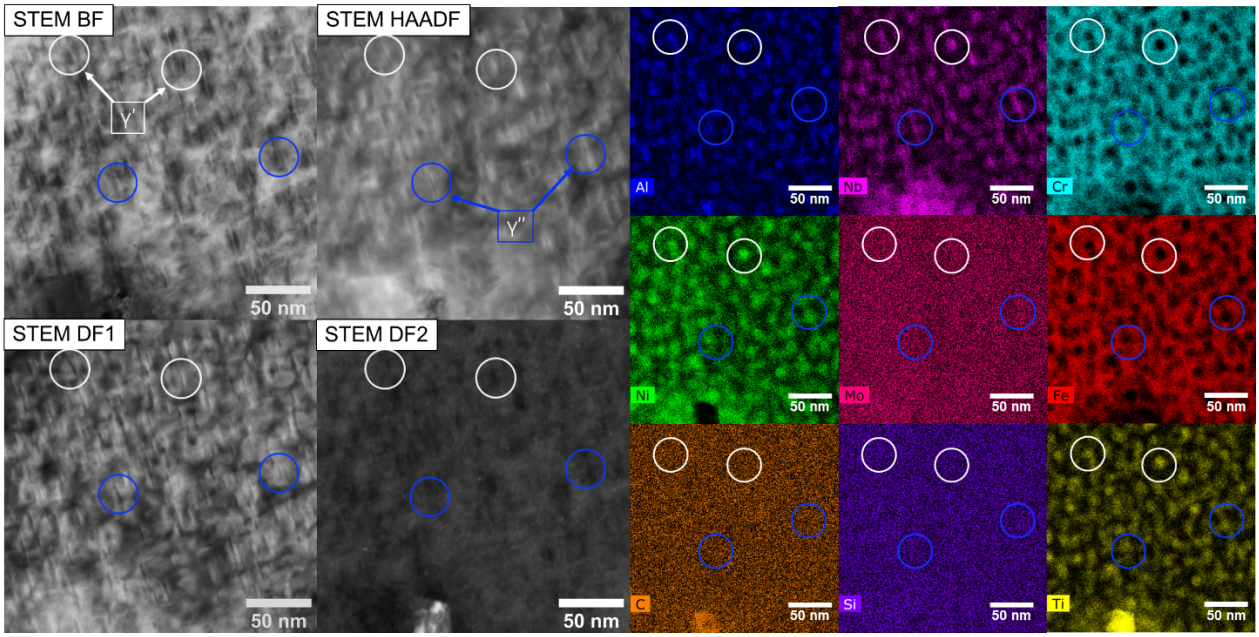

Figure 7. Higher magnification STEM images of ASB AM Superalloy 718 with corresponding EDS maps for precipitate forming elements showing γ′ (Ni_3[Ti,Al]) circled in white and γ″ (Ni_3Nb) precipitates circled in blue. For interpretation of the references to color in this figure, the reader is referred to the web version of this article.

Table 3. Summary of characterization results for precipitate phases observed in ASB AM718. The error in number densities is the minimum of error from counting statistics [48] or from the TEM foil thickness measurement. *N.O.* indicates that the feature was not observed.

Alloy designation	Feature	Number of features observed	Percent of total precipitation (%)	Mean eq. diameter (nm)	Standard error of mean (nm)	Number density (m^{-3})
AM718-ASB-1	γ'	571	16.08	8.34	0.11	$2.68 \pm 0.3 \times 10^{21}$
	γ"	2,484	69.94	9.47	0.14	$1.17 \pm 0.1 \times 10^{22}$
	δ	467	13.15	9.89	0.55	$2.19 \pm 0.2 \times 10^{21}$
	Laves	7	0.20	77.25	9.9	$3.29 \pm 0.6 \times 10^{19}$
	Carbides	15	0.42	27.52	2.7	$7.04 \pm 0.9 \times 10^{19}$
	Pores	10	-	12.49	1.3	$4.70 \pm 0.8 \times 10^{19}$
	Oxide	7	0.20	25.65	6.2	$3.29 \pm 0.8 \times 10^{19}$
AM718-ASB-2	γ'	247	8.27	10.59	0.21	$1.16 \pm 0.2 \times 10^{21}$
	γ"	2,570	86.01	10.05	0.09	$1.21 \pm 0.1 \times 10^{22}$
	δ	156	5.22	14.34	1.9	$7.33 \pm 0.9 \times 10^{20}$
	Laves	9	0.30	51.56	14.9	$4.23 \pm 0.4 \times 10^{19}$

	Carbides	N.O.	-	-	-	-
	Pores	26	-	9.24	0.44	$1.27 \pm 0.3 \times 10^{20}$
	Oxide	7	0.20	14.3	6.7	$2.82 \pm 0.6 \times 10^{19}$

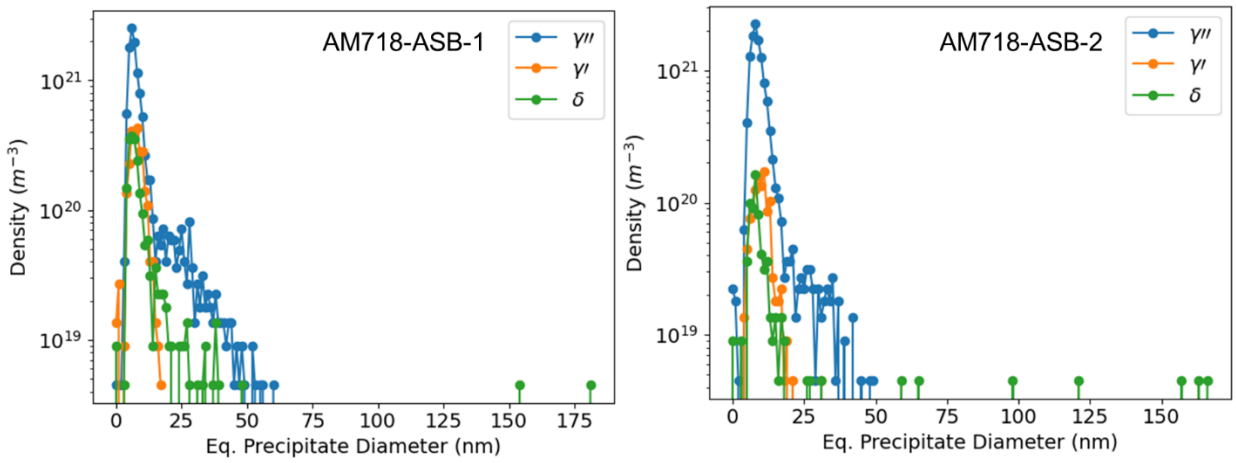

Figure 8. Precipitate size distributions for γ′, γ″, and δ phases in ASB AM Superalloy 718.

The microstructure found in the heat-treated specimens was not as complex as the ASB AM718. Representative STEM HAADF images for the wrought alloy 718 and the three heat treatments of AM718 are shown in Figure 9. The wrought alloy contained the expected microstructure that consists of a high density of fine γ′ and γ″ precipitates, consistent with the ASTM-prescribed microstructure for precipitate-hardened superalloys [33]. Following the homogenization treatment to produce AM718-HM, the microstructure consisted of a low density of remaining oxide and carbide particles and dissolved all Laves, δ, γ′, or γ″ phases present in the ASB AM718. After aging, the AM718-HT1 and AM718-HT2 treatments appeared qualitatively similar and contained a high density of fine γ′, γ″, and δ precipitates, with AM718-HT2 having greater precipitate densities overall. However, AM718-HT1 contained a higher fraction of δ phase, as expected from the heat treatment. The quantitative analysis of γ′, γ″, and δ particles is provided in Table 4, and the size distribution of γ′, γ″, and δ precipitates from each heat treatment is shown in Figure 10.

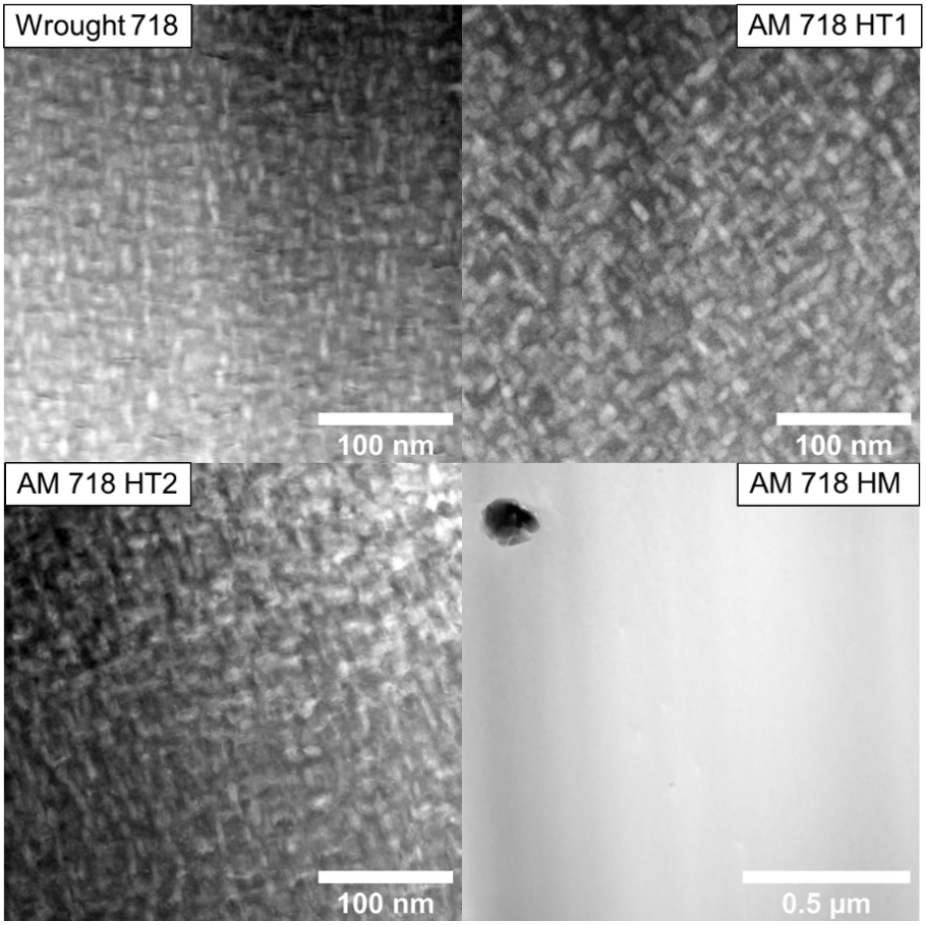

Figure 9. STEM HAADF images of wrought alloy 718, AM718-HT1, AM718-HT2, and AM718-HM showing the mixture of γ′, γ″, and δ as bright features and oxides as dark features.

Table 4. Summary of characterization results for precipitate phases observed in heat-treated AM718 and W718. The error in number densities is the minimum of error from counting statistics [48] or from the TEM foil thickness measurement. *N.O.* indicates that the feature was not observed. *N/A* indicates there was not enough of the feature to calculate this value.

Alloy designation	Feature	Number of features observed	Percent of total precipitation (%)	Mean eq. diameter (nm)	Standard error of mean (nm)	Number density (m^{-3})
AM718-HT1	γ'	407	7.39	8.16	0.09	$1.91 \pm 0.2 \times 10^{21}$
	γ"	4,615	83.74	8.93	0.04	$2.17 \pm 0.2 \times 10^{22}$
	δ	487	8.84	8.17	0.08	$2.29 \pm 0.2 \times 10^{21}$
	Laves	N.O.	-	-	-	-
	Carbides	2	0.04	35.2	14.4	$9.39 \pm 1.2 \times 10^{18}$
	Pores	N.O.	-	-	-	-
	Oxide	N.O.	-	-	-	-
AM718-HT2	γ'	846	9.93	6.80	0.073	$3.97 \pm 0.4 \times 10^{21}$
	γ"	7,208	84.59	7.72	0.024	$3.39 \pm 0.3 \times 10^{22}$
	δ	466	5.47	7.06	0.062	$2.19 \pm 0.2 \times 10^{21}$
	Laves	N.O.	-	-	-	-
	Carbides	1	0.01	63.59	N/A	$4.70 \pm 2.4 \times 10^{18}$
	Pores	N.O.	-	-	-	-
	Oxide	N.O.	-	-	-	-
AM718-HM-1	γ'	N.O.	-	-	-	-
	γ"	N.O.	-	-	-	-
	δ	N.O.	-	-	-	-
	Laves	N.O.	-	-	-	-
	Carbides	3	75.00	45.79	13.7	$1.41 \pm 0.5 \times 10^{19}$
	Pores	N.O.	-	-	-	-
	Oxide	1	25.00	135.89	N/A	$4.70 \pm 2.4 \times 10^{18}$
AM718-HM-2	γ'	N.O.	-	-	-	-
	γ"	N.O.	-	-	-	-
	δ	N.O.	-	-	-	-
	Laves	N.O.	-	-	-	-
	Carbides	4	66.67	81.83	49.5	$1.88 \pm 0.6 \times 10^{19}$
	Pores	1	-	11.10	N/A	$4.70 \pm 2.4 \times 10^{18}$
	Oxide	2	33.33	47.33	40.9	$9.39 \pm 1.8 \times 10^{18}$
W718-Z1653	γ'	528	4.38	5.6	0.065	$2.38 \pm 0.25 \times 10^{21}$
	γ"	7735	64.28	5.9	0.015	$3.48 \pm 0.38 \times 10^{22}$
	δ	3770	31.33	5.9	0.019	$1.69 \pm 1.8 \times 10^{22}$
	Laves	N.O.	-	-	-	-
	Carbides	N.O.	-	-	-	-
	Pores	N.O.	-	-	-	-
	Oxide	N.O.	-	-	-	-

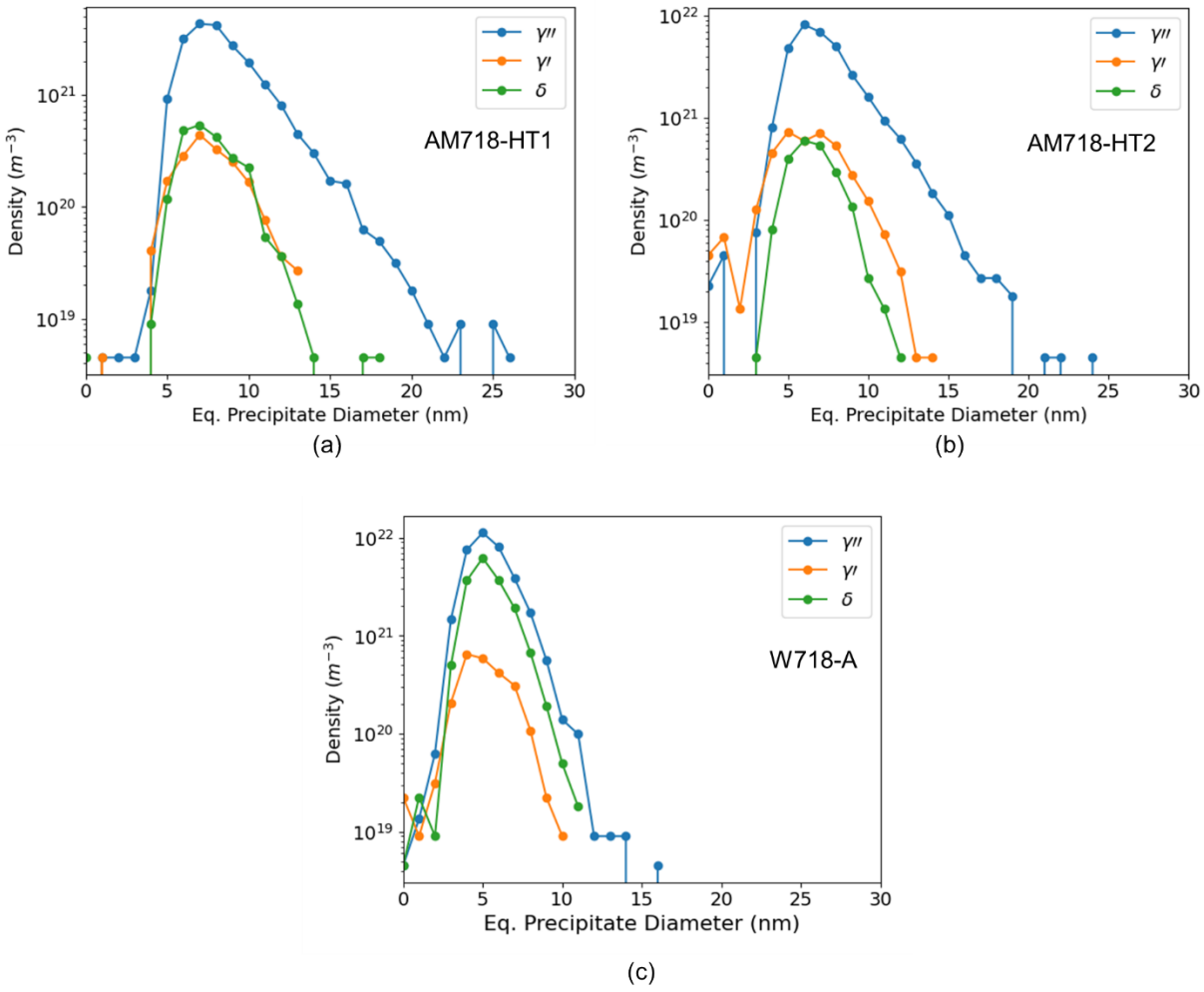

278

279 **Figure 10. Precipitate size distributions for γ′, γ″, and δ phases in (a,b) heat-treated AM alloy 718 and (c) W718.**

280

281 3.3 Tensile test results up to 600 °C

282 Representative engineering stress-strain curves for each heat treatment of AM718 and the reference
283 wrought alloy 718, labeled as W718, strained at each test temperature, are shown in Figure 11, and the
284 stress-strain curves for each strained specimen are provided in the supplementary materials. Engineering
285 stress-strain curves for each strained specimen from each condition are displayed in the appendix as Figure
286 A.14 through Figure A.17 for transparency. These curves were used to calculate the common engineering
287 properties of elastic modulus, 0.2% offset yield strength, uniform elongation, ultimate tensile stress, total
288 elongation, and fracture strength. These properties are included in Table 5. Although acoustic methods are

preferred for determining the elastic modulus, the elastic modulus here was calculated by fitting a line to the elastic portion of each tensile curve, minimizing the least squares error, and extracting the slope of the line through a simple Hooke's Law approximation.

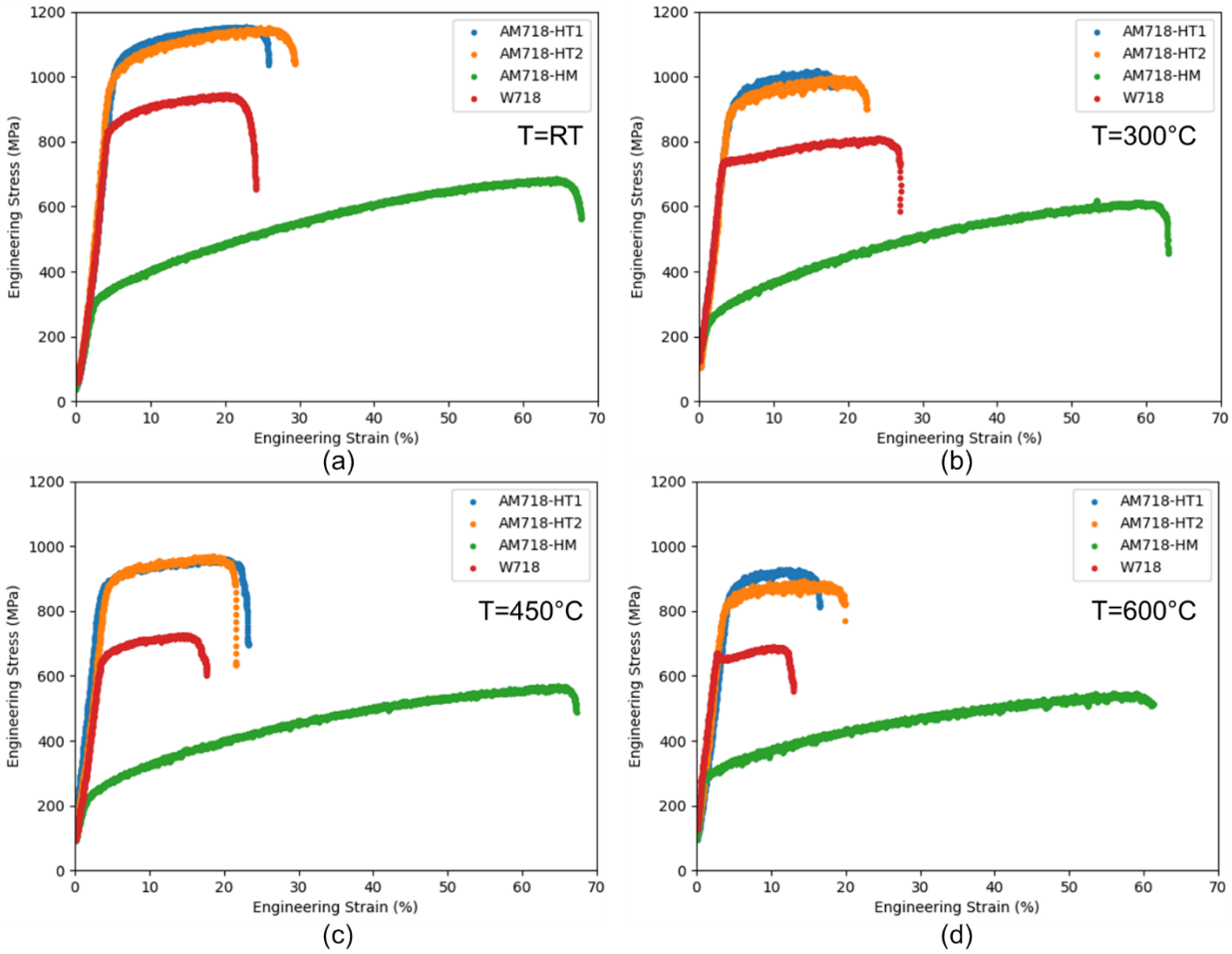

Figure 11. Representative engineering stress-strain curves for heat–treated AM alloy 718 and wrought alloy 718 at (a) room temperature, (b) 300 °C, (c) 450 °C, and (d) 600 °C.

295 **Table 5. Engineering properties derived from room temperature tensile tests of wrought alloy 718 and heat-treated AM**

296 **alloy 718.** Values reported are the averages of all tested specimens and their associated standard deviations.

Designation	Test temp. (°C)	Elastic modulus (GPa)	0.2% offset yield (MPa)	Uniform elongation (%)	Ultimate tensile strength (MPa)	Total Elongation (%)	Fracture Strength (MPa)
AM718-HT1	22	244 ± 19.9	1056 ± 13.6	14.6 ± 1.9	1,187 ± 17.7	26.1 ±1.7	1007 ± 45.0
	300	223 ± 11.5	843 ± 68.0	9.99 ± 1.9	1,011 ± 17.9	19.6 ± 2.1	930 ± 48.3
	450	230.6 ± 21.3	836 ± 53.5	11.7 ± 2.2	959 ± 23.1	23.2 ± 0.8	834 ± 118
	600	227 ± 22.1	810 ± 17.0	7.1 ± 1.2	896 ± 9.22	16.3 ± 1.2	789 ± 15.1
AM718-HT2	22	234 ± 11.8	978 ± 33.2	18.5 ± 2.7	1,144 ± 18.6	28.6 ± 3.3	1008 ± 24.3
	300	240 ± 7.6	852 ± 22.7	15.9 ± 3.3	987 ± 12.7	24.6 ± 3.4	888 ± 22.9
	450	226.1 ± 11.9	825 ± 45.5	11.0 ± 1.9	945 ± 12.9	22.3 ± 1.5	806 ± 102
	600	230 ± 8.2	789 ± 33.0	7.9 ± 2.2	876 ± 23.4	17.1 ± 1.5	770 ± 26.1
AM718-HM	22	131 ± 6.1	338 ± 14.8	54.1 ± 1.2	717 ± 20.3	67.5 ± 1.5	552 ± 26.1
	300	119 ± 44	303 ± 14.7	58.3 ± 5.8	610 ± 12.4	63.8 ± 4.4	463 ± 36.8
	450	100.3 ± 15.4	294 ± 48.0	47.6 ± 5.1	563 ± 9.22	66.7 ± 3.7	478 ± 10.8
	600	148 ± 27	250 ± 9.39	53.6 ± 4.6	517 ± 16.4	62.5 ± 3.5	423 ± 51.4
W718-Z1653	22	215 ± 23.0	759 ± 114	14.9 ± 1.8	928 ± 37.2	24.4 ± 1.3	734 ± 77.7
	300	217 ± 3.5	711 ± 28.6	13.8 ± 4.8	802 ± 25.3	22.6 ± 6.0	585 ± 97.8
	450	190.5 ± 18.5	666 ± 14.0	8.4 ± 4.1	719 ± 30.8	17.5 ± 3.8	574 ± 21.9
	600	179 ± 18.8	653 ± 13.5	6.0 ± 1.9	697 ± 21.8	14.3 ± 2.3	521 ± 40.7

297

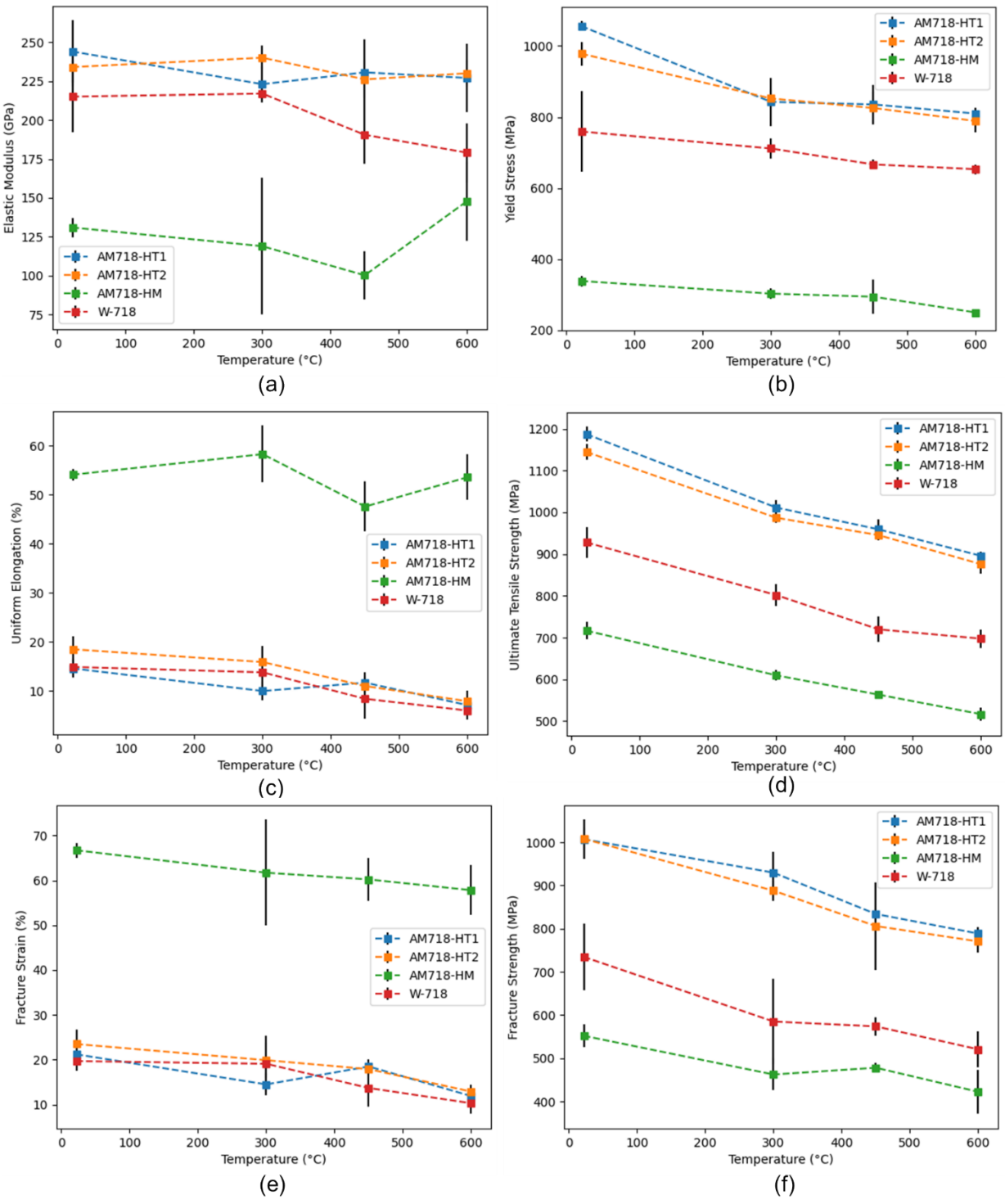

298

299 **Figure 12. Engineering properties for heat-treated AM718 and W718 as a function of testing temperature: (a) elastic**

300 **modulus, (b) yield stress, (c) uniform elongation, (d) ultimate tensile strength, (e) total elongation, and (f) fracture strength.**

301

4. Discussion

4.1 Comparison of Wrought and AM 718

The wrought superalloy 718 displayed the expected behavior for a precipitate-hardened alloy consisting of a large yield stress and a high ultimate tensile stress. However, both the yield and ultimate tensile stress were 15–20% lower than expected for the ASTM heat treatment [1,8], and both had an increased uniform elongation and fracture strain compared with results presented in the literature [8,46,49]. The increased fracture strain is consistent with the expectation of subsize specimens and may result from the decrease in scale factor [35]. A fraction of the metastable γ″ transformed into intragranular δ-phase precipitates as predicted by the time-temperature-transformation diagram [45], and over-aging as discussed in Appendix A.2. Although δ precipitates share the composition of Ni_3Nb with γ″, the lattice-precipitate interface is incoherent for the δ-phase, thus reducing its contribution to strength [8]. The high density of δ precipitates (Table 4) in the wrought superalloy 718 likely reduced the strength of the alloy compared to the expected ASTM-designated strength.

Prior to heat treatments, there was a clear preferred grain orientation in the as-built condition relative to the build direction. This likely would result in anisotropic properties. However, the first step of the heat treatment was a high temperature solution anneal meant to remove all previous precipitation. This resulted in significant grain growth, as expected for annealing above 982 °C [50], and a transition from lath-like elongated grains to more equiaxed grains, as expected for the recrystallization regime from 900 to 1066 °C [50].Likely as a result, the yield strength and ultimate tensile strength of AM718-HT1 and AM718-HT2 (Table 2) increased relative to W718 and were well within ASTM specifications of superalloy 718. The AM718-HT2 condition displayed a larger uniform elongation after yield compared with the AM718-HT1 condition. Comparison of the microstructures of these two conditions as presented in Table 4, both exhibited a high density of γ″ precipitates on the order of 10^{22} m^{-3}, with AM718-HT-2 having a larger density. However, AM718-HT1 had a higher fraction of the δ-phase, which likely contributed to the

decrease in uniform elongation. The agreement in the uniform elongation between AM718-HT-1 and W718 lends support to the detrimental effects of δ-phase precipitates observed in W718.

When the precipitates were removed through homogenization and solution annealing (AM718-HM), the yield stress and ultimate tensile strength decreased with a significantly greater uniform elongation and fracture strain, which is consistent with solution-annealed alloy 718 [51]. However, the elastic modulus was significantly lower than the 190–220 GPa range expected for polycrystalline pure Ni [52], stemming from the decrease in yield stress. In the literature, a decreased elastic modulus was found when annealing at high temperatures for 1 h to achieve values of 165–172 GPa [53–58]. Increasing the annealing temperature reduced the elastic modulus linearly and correlated with an increase in the grain size [55]. Compared with these previous works, the homogenization treatment in this work was performed for a much longer time and at higher temperatures. In this work, the recrystallized, homogenized AM718-HM still had a reduced grain size compared to that of the wrought alloy, but without precipitates, making the implied relationship between grain size and elasticity unclear. Additionally, at 600 °C, the elastic modulus appeared to increase for AM718-HM. While precipitation is not expected based on the TTT diagram (Figure 1b), solute clustering is likely occurring. Many precipitating phases proceed along a mechanism consisting of clustering of the constituent elements and accumulation of solutes until a critical concentration then transition to a distinct phase [59–61]. Therefore, the elastic modulus increase may stem from dislocation pinning on solute clusters that have not transitioned into γ′ or γ″ precipitates. These clusters were not visible in the STEM EDS datasets and thus may reside below the resolution of the technique estimated at approximately 2 nm for the parameters presented in the Methodology. An approach is needed to deconvolute the contributions of grain size, precipitates, and other features contributing to the yield strength.

4.2 Microstructure-Property Relationships

There is an inherent link between a material's microstructure and macroscopic mechanical properties. In the broadest sense, the yield strength of a material is the sum of the inherent strength from the crystal lattice, $\sigma_{Y,0}$, with additional strength from the effects of defects and secondary phases, σ_D, interpreted through a classical Orowan dislocation bowing process [62]. The inherent strengthening shown in Eq. (2) stems from (1) the solid solutioning strength from substitutional elements in the face-centered cubic (FCC) Ni lattice, σ_{SS}; (2) the grain boundaries through the Hall-Petch relationship, $\frac{k_y}{\sqrt{d}}$, where k_y is a constant, and d is the grain diameter; and (3) the dislocation friction stress, also known as the Peierls-Nabarro stress, τ_{P-N} [63]. The impact of defects and precipitates is generally described by a dispersed barrier hardening model, as shown in Eq. (3): $\alpha_i M \mu b \sqrt{N_i d_i}$, where α represents the strength of the barrier, M is the Taylor factor, μ is the shear modulus, b is the Burgers vector, N is the density of the precipitates, and d is their size described as an equivalent diameter:

$$\sigma_Y = \sigma_{SS} + \tau_{P-N} + \frac{k_y}{\sqrt{d}} + \sum_i^{\delta,\gamma',\gamma'',MX,oxide} \alpha_i M \mu b \sqrt{N_i d_i}. \quad (3)$$

A linear superposition was utilized because the contributions from each component are not expected to be similar in strength. Because W718 and each heat treatment of AM718 all exhibited similar microstructure features, all yield stress measurements were made into a linear system of equations to solve for the contributions of each component of the microstructure to the strength. Because of the low density of carbides and oxides, these features were assumed to contribute a negligible amount of strength compared to the other factors and were excluded from the analysis. The solid solution strengthening and the dislocation friction stress were grouped together and assumed to act together linearly. The median grain diameter was used instead of the average to reduce the influence of outliers. Rather than assume an average density and diameter, the precipitate size distributions shown in Figure 10 were integrated to be included in the dispersed barrier calculations. M is 3.06 [64], whereas the Burgers vector was assumed to be equal to the lattice parameter for FCC nickel. This results in a linear system of equations with 5 unknown variables ($\sigma_{SS} + \tau_{P-N}$, k_y, $\alpha_{\gamma'}$, $\alpha_{\gamma''}$ and α_δ) for each of the 16 yield stress measurements given in Table 5. Assuming

that the inherent strengthening and grain boundary contributions are the same for each measurement of the same heat treatment, the system reduces the system to 16 equations with 28 unknowns—an underdetermined system. In many similar analyses, the barrier strength is assumed to be independent of temperature for each feature, which would reduce the system to 16 equations with 7 unknowns and would become overdetermined. An overdetermined system almost always yields inconsistent solutions when constructed with randomly determined starting points for each variable. Although an underdetermined system cannot be solved for a unique solution, the Moore-Penrose pseudoinverse of the linear coefficient matrix of the unknowns can be used to construct a linear solution that minimizes the least-squares approximation. The coefficients found from this solution are displayed in Table 6. An alternative approach using theoretical strength factors from Tan and Busby [65] is presented in the Appendix for reference and suggests similar values for α as this discussion.

Table 6. Coefficients determined to correlate microstructure to yield strength with linear least squares error.

Temperature (°C)	T/T_m	Solid solution + friction stress modifier, C_1 (×1 MPa)	Hall-Petch coefficient, k_y (MPa×m$^{1/2}$)	α for γ″ (unitless)	α for δ (unitless)
22	0.17	0 (see text)	1,716,711	0.129	0.129
300	0.33	236.24	484,541	0.131	0.057
450	0.42	134.46	882,908	0.118	0.078
600	0.50	56.35	1,000,045	0.112	0.111

Lucas [66] summarizes the reported α values of different types of defects and categorizes them into three groups: (1) weak barriers such as small bubbles/loops and dislocations with $\alpha < 0.25$, (2) intermediate barriers such as Frank loops and small precipitates with $0.33 < \alpha < 0.45$, and (3) strong barriers such as voids and large precipitates with α~1 obstacles. According to this interpretation, the precipitates examined are all weak barriers with a variable strength coefficient based on temperature. All materials exhibit several major temperature regimes separated by the onset of migration of point defects. In pure nickel, vacancy defects are immobile below about 77–100 °C, whereas small interstitial clusters and interstitial-solute clusters may migrate [67]. Thus, the tensile tests at room temperature can be considered as testing the resistance of each class of microstructural features to primarily stress-driven interstitial dislocation motion. The results in Table 6 suggest that the main contributions to yield strength at room temperature are grain

boundaries, γ″, and δ precipitates, with the γ″ and δ exhibiting the same obstacle strength. However, when the tensile temperature is increased above the onset of vacancy mobility, the strength coefficient for γ″ precipitates remain about the same as at room temperature but decreases for δ phase. Because 300 °C is still a relatively low temperature and is unlikely to have a significant thermal concentration of vacancies, this reduction in the strength of δ can be attributed to the increase in interstitial motion between room temperature and 300 °C. With increasing temperature up to 600 °C and corresponding increase in thermal contributions to interstitial motion and vacancy concentration, the strengthening coefficient for γ" decreases, and δ increases until these precipitate phases become equal strength. Both phases are the same chemical composition of Ni_3Nb, but the disk-shaped γ″ precipitates are coherent with the nickel lattice on {100} planes, maintaining the c-axis perpendicular to the disks, whereas the δ phase is semi-coherent [49], possibly driving the differences in the observed strengthening factors when thermal motion is considered. Coherent precipitates produce larger long-range strain fields compared to semi-coherent precipitates, and thus they also increase the combined mechanical and thermal work required to overcome a barrier. If the required work is sufficiently small, then thermal vibrations of the lattice may assist dislocations to pass through a weak strain field and overcome the precipitate [68]. Atomistic simulations of point defect and dislocation interactions with these precipitates would provide strong additional insight into the role of precipitate coherency on strength at high temperatures.

With these coefficients, the relative contribution of each term to the total yield strength can be estimated and is displayed as a percentage in Figure 13. Based on this analysis, several trends are visible, and general processes can be proposed. At room temperature, the grain boundaries appear to be responsible for most of the strength from the lattice (AM718-HM), whereas the precipitates contribute more than half of the yield strength (AM718-HT1, AM718-HT2, and W718). However, this result is counterintuitive because some contribution from solutes in the lattice would be expected. Assuming primarily stress-driven dislocation motion, these results suggest that the stresses necessary to eject dislocations from grain boundaries are significantly higher than those necessary to overcome small interstitial solutes or solutes in solution. Therefore, motion around solutes is comparatively trivial and results in an apparent lack of

strengthening from these features. As temperature increases to 300 °C, interstitials have more thermal motion, and solutes in the matrix provide pinning sites and increase the relative contribution to the yield strength. However, as temperature increases even further, it becomes easier to bypass the solutes, and the grain boundaries once again become a relatively stronger barrier to overcome. The main assumption in the Hall-Petch slope (k_y) is that it is proportional to the work required to eject dislocations from grain boundaries [69], and thus the trends in Table 6 and Figure 13 suggest a strong reliance on interstitial motion, similar to the discussion surrounding δ phase precipitates in the preceding paragraph. At all temperatures, the relative contribution to the yield strength from γ″ remained consistent between 48–57% of the total strength, indicating the utility of this phase to the high-temperature strength of superalloy 718. One drawback from this analysis is that the contributions of other microstructural features such as carbides, oxides, and γ' precipitates could not be assessed because of their lower density and apparent strength.

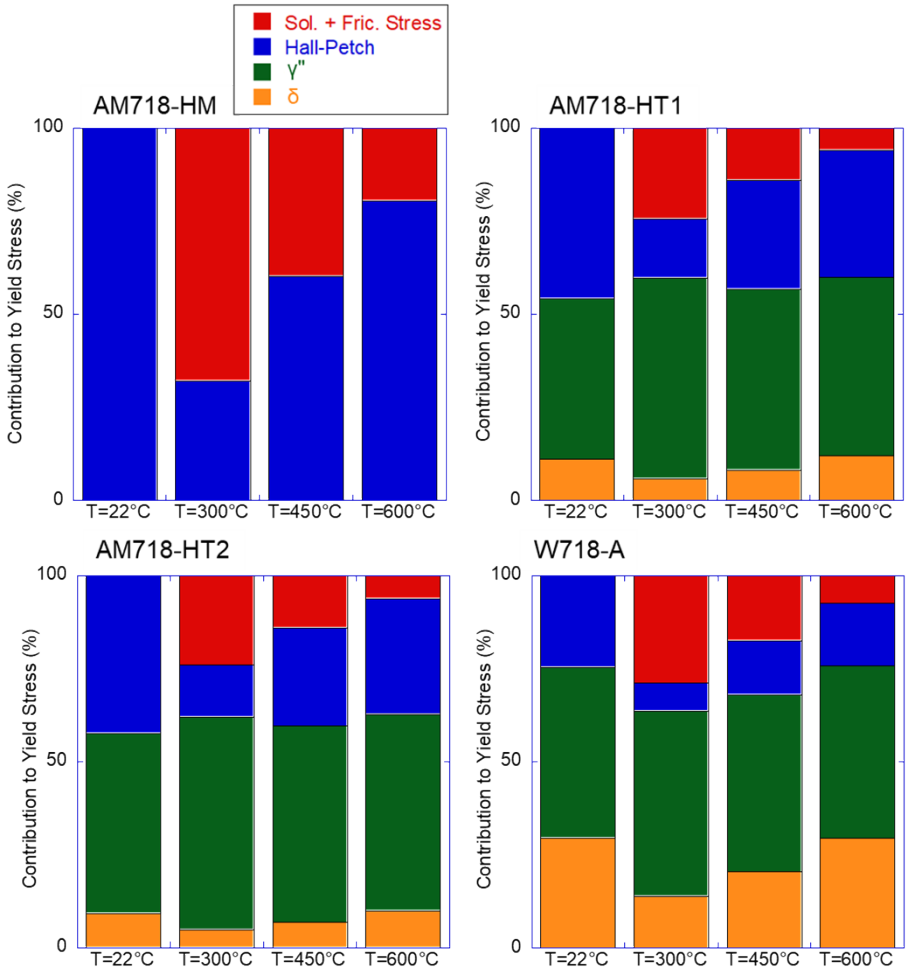

Figure 13. Fractional contribution to the yield strength from solid solution strengthening and friction strength, grain boundaries through the Hall-Petch relationship, γ" precipitates, and δ precipitates for each heat treatment of superalloy 718 examined in this work.

While many researchers investigated the relationships between post-build heat treatments, mechanical response, and microstructure of superalloy 718, the results tend to focus more on the room temperature properties and semi-empirical relationships. However, superalloy 718 is used in many applications up to its high creep-rupture strength, which limits its use at high temperatures near 650 - 700 °C. This is believed to stem from the coarsening of the γ″ precipitates [8] expected from the TTT diagram (Figure 1b). Because of the wide temperature range in the derivation and relative simplicity of the dispersed barrier model produced in this work, it can easily integrate into modeling and simulation workflows to estimate the yield strength of AM superalloy 718 components after fabrication. Such projects, for example the ExaAM initiative [70], are expected to transform AM through high performance computing (exascale) simulation of the complex interplay between the physical phenomena (e.g., heat transfer, melting, solidification, fluid flow) involved in the additive process to simulate the microstructure and resulting properties. Because the precipitation in superalloy 718 is strongly sensitive to the thermal history, having a microstructure-strength relationship dependent on the precipitate size, precipitate density, and morphology will significantly improve the quality of efforts to simulate the properties of traditional and AM components.

5. Conclusions

Microstructure characterization and baseline mechanical testing were performed on additively manufactured superalloy 718 produced via PBF-LB. The key findings and conclusions derived from this work are summarized as follows.

The microstructure of as-built superalloy 718 contained many of the phases predicted from the isothermal phase diagram with strong variation, depending on the location in the part at nano- to micro-scales. The formation of Laves and on-boundary δ phase suggests that the mechanical properties would

result in poor performance of the as-built component, whereas the lath-like structure suggests that the mechanical properties would strongly depend on orientation. Purely based on the as-built microstructure, superalloy 718 is not recommended for structural use without post-build heat treatments using these processing parameters.

Three heat treatments consisting of two step homogenization, solution treatment, and aging were employed to control the precipitate morphology in additively manufactured superalloy 718 after fabrication. The yield strength and ultimate tensile strength of the heat treated additively manufactured superalloy 718 increased relative to the wrought 718 and were well within ASTM specifications for superalloy 718. Both HT-1 and HT-2 treatments resulted in a high density of γ″ precipitates on the order of 10^{22} m^{-3}, with AM718-HT-2 having a larger density and a lower fraction of intragranular δ-phase. Interpreting the yield strength through an Orowan dislocation mechanism determined that all precipitates analyzed in this work proved to be weak barriers to dislocation motion, but they provided strength to the alloy through their consistent high density. At temperatures ranging from 22 to 600 °C, the relative contribution to the yield strength from γ″ remained consistent between 48–57% of the total strength, indicating the utility of this phase to the high-temperature strength of superalloy 718. The strength factors for γ″ and δ precipitates were found to trend inversely with tensile test temperature and may be attributable to the differences in precipitate coherency. From the homogenized condition, it is suggested that the contributions in strength from solutes and grain boundaries are strongly temperature dependent. Based on the results of this study, a high-temperature homogenization followed by a traditional ASTM aging, designated *HT-2* in this work, is recommended to recover the properties and microstructure from additively manufactured superalloy 718 necessary for high-temperature strength. Because of the wide temperature range in the derivation and relative simplicity of the dispersed barrier model produced in this work, it can easily be integrated into modeling and simulation workflows to estimate the yield strength of traditional and AM components.

6. Acknowledgments

This research was sponsored in part by the Laboratory Directed Research and Development Program of Oak Ridge National Laboratory, managed by UT-Battelle, LLC, for the US Department of Energy. This research was supported by the Transformational Challenge Reactor/Advanced Materials and Manufacturing Technologies program supported by the US Department of Energy, Office of Nuclear Energy. T. Austin's contributions are based on work supported under a US Department of Energy Office of Nuclear Energy Integrated University Program Graduate Fellowship. SEM and STEM characterization were performed in the Low Activation Materials Development and Analysis laboratory at ORNL. Additional acknowledgments are extended for Keith Carver for operating the Concept X-Line 2000R, Tom Geer and Gavin Mattingly for sample preparation, Eric Manneschmidt for performing the tensile tests, and T. S. Byun and Holden Hyer for thoughtful feedback.

7. CRediT statement

Stephen Taller – Conceptualization, Methodology, Software, Formal analysis, Investigation, Visualization, Writing - Original Draft, Project administration

Ty Austin – Software, Formal analysis, Investigation, Writing - Review and Editing

8. References

[1] T. Yonezawa, Nickel-Based Alloys, in: Compr. Nucl. Mater., Elsevier, 2020: pp. 319–354. https://doi.org/10.1016/B978-0-12-803581-8.00676-7.

[2] M.J. Donachie, S.J. Donachie, Superalloys: A Technical Guide, 2nd Edition, 2nd Editio, ASM International, 2002.

[3] M. Griffiths, Ni-based alloys for reactor internals and steam generator applications, in: Struct. Alloy. Nucl. Energy Appl., Elsevier Inc., 2019: pp. 349–409. https://doi.org/10.1016/B978-0-12-397046-6.00009-5.

[4] E. Paccou, M. Mokhtari, C. Keller, J. Nguejio, W. Lefebvre, X. Sauvage, S. Boileau, P. Babillot, P. Bernard, E. Bauster, Investigations of powder reusing on microstructure and mechanical

properties of Inconel 718 obtained by additive manufacturing, Mater. Sci. Eng. A. 828 (2021) 142113. https://doi.org/10.1016/j.msea.2021.142113.

[5] A. Hilaire, E. Andrieu, X. Wu, High-temperature mechanical properties of alloy 718 produced by laser powder bed fusion with different processing parameters, Addit. Manuf. 26 (2019) 147–160. https://doi.org/10.1016/j.addma.2019.01.012.

[6] E.M. Fayed, M. Saadati, D. Shahriari, V. Brailovski, M. Jahazi, M. Medraj, Effect of homogenization and solution treatments time on the elevated-temperature mechanical behavior of Inconel 718 fabricated by laser powder bed fusion, Sci. Rep. 11 (2021) 2020. https://doi.org/10.1038/s41598-021-81618-5.

[7] R. Firoz, S.K. Basantia, N. Khutia, H.N. Bar, S. Sivaprasad, G.V.S. Murthy, Effect of microstructural constituents on mechanical properties and fracture toughness of Inconel 718 with anomalous deformation behavior at 650 °C, J. Alloys Compd. 845 (2020) 156276. https://doi.org/10.1016/j.jallcom.2020.156276.

[8] D.D. Keiser, H.L. Brown, Review of the physical metallurgy of Alloy 718, U.S. Department of Energy, 1976. https://doi.org/10.2172/4016087.

[9] K. Moussaoui, W. Rubio, M. Mousseigne, T. Sultan, F. Rezai, Effects of Selective Laser Melting additive manufacturing parameters of Inconel 718 on porosity, microstructure and mechanical properties, Mater. Sci. Eng. A. 735 (2018) 182–190. https://doi.org/10.1016/j.msea.2018.08.037.

[10] Y. Gao, D. Zhang, M. Cao, R. Chen, Z. Feng, R. Poprawe, J.H. Schleifenbaum, S. Ziegler, Effect of δ phase on high temperature mechanical performances of Inconel 718 fabricated with SLM process, Mater. Sci. Eng. A. 767 (2019) 138327. https://doi.org/10.1016/j.msea.2019.138327.

[11] L. Huang, Y. Cao, J. Zhang, X. Gao, G. Li, Y. Wang, Effect of heat treatment on the microstructure evolution and mechanical behaviour of a selective laser melted Inconel 718 alloy, J. Alloys Compd. 865 (2021) 158613. https://doi.org/10.1016/j.jallcom.2021.158613.

[12] J.R. Zhao, F.Y. Hung, T.S. Lui, Microstructure and tensile fracture behavior of three-stage heat treated inconel 718 alloy produced via laser powder bed fusion process, J. Mater. Res. Technol. 9

(2020) 3357–3367. https://doi.org/10.1016/j.jmrt.2020.01.030.

[13] M.M. Kirka, F. Medina, R. Dehoff, A. Okello, Mechanical behavior of post-processed Inconel 718 manufactured through the electron beam melting process, Mater. Sci. Eng. A. 680 (2017) 338–346. https://doi.org/10.1016/j.msea.2016.10.069.

[14] E. Hosseini, V.A. Popovich, A review of mechanical properties of additively manufactured Inconel 718, Addit. Manuf. 30 (2019) 100877. https://doi.org/10.1016/j.addma.2019.100877.

[15] F. Liu, F. Lyu, F. Liu, X. Lin, C. Huang, Laves phase control of inconel 718 superalloy fabricated by laser direct energy deposition via $δ$ aging and solution treatment, J. Mater. Res. Technol. 9 (2020) 9753–9765. https://doi.org/10.1016/j.jmrt.2020.06.061.

[16] S. Sui, C. Zhong, J. Chen, A. Gasser, W. Huang, J.H. Schleifenbaum, Influence of solution heat treatment on microstructure and tensile properties of Inconel 718 formed by high-deposition-rate laser metal deposition, J. Alloys Compd. 740 (2018) 389–399. https://doi.org/10.1016/j.jallcom.2017.11.004.

[17] X. Li, J.J. Shi, C.H. Wang, G.H. Cao, A.M. Russell, Z.J. Zhou, C.P. Li, G.F. Chen, Effect of heat treatment on microstructure evolution of Inconel 718 alloy fabricated by selective laser melting, J. Alloys Compd. 764 (2018) 639–649. https://doi.org/10.1016/j.jallcom.2018.06.112.

[18] X. Yu, X. Lin, F. Liu, L. Wang, Y. Tang, J. Li, S. Zhang, W. Huang, Influence of post-heat-treatment on the microstructure and fracture toughness properties of Inconel 718 fabricated with laser directed energy deposition additive manufacturing, Mater. Sci. Eng. A. 798 (2020) 140092. https://doi.org/10.1016/j.msea.2020.140092.

[19] C.E. Seow, H.E. Coules, G. Wu, R.H.U. Khan, X. Xu, S. Williams, Wire + Arc Additively Manufactured Inconel 718: Effect of post-deposition heat treatments on microstructure and tensile properties, Mater. Des. 183 (2019) 108157. https://doi.org/10.1016/j.matdes.2019.108157.

[20] S. Sui, J. Chen, Z. Li, H. Li, X. Zhao, H. Tan, Investigation of dissolution behavior of laves phase in inconel 718 fabricated by laser directed energy deposition, Addit. Manuf. 32 (2020) 101055. https://doi.org/10.1016/j.addma.2020.101055.

562 [21] S. Sui, H. Tan, J. Chen, C. Zhong, Z. Li, W. Fan, A. Gasser, W. Huang, The influence of Laves
563 phases on the room temperature tensile properties of Inconel 718 fabricated by powder feeding
564 laser additive manufacturing, Acta Mater. 164 (2019) 413–427.
565 https://doi.org/10.1016/j.actamat.2018.10.032.
566 [22] M.J. Sohrabi, H. Mirzadeh, M. Rafiei, Solidification behavior and Laves phase dissolution during
567 homogenization heat treatment of Inconel 718 superalloy, Vacuum. 154 (2018) 235–243.
568 https://doi.org/10.1016/j.vacuum.2018.05.019.
569 [23] B.B. Babamiri, J. Indeck, G. Demeneghi, J. Cuadra, K. Hazeli, Quantification of porosity and
570 microstructure and their effect on quasi-static and dynamic behavior of additively manufactured
571 Inconel 718, Addit. Manuf. 34 (2020). https://doi.org/10.1016/j.addma.2020.101380.
572 [24] G.M. Volpato, U. Tetzlaff, M.C. Fredel, A comprehensive literature review on laser powder bed
573 fusion of Inconel superalloys, Addit. Manuf. (2022) 102871.
574 https://doi.org/10.1016/j.addma.2022.102871.
575 [25] J.M. Poole, K.R. Stultz, J.M. Manning, The Effect of INGOT Homogenization Practice on the
576 Properties of Wrought Alloy 718 and Structure, in: Superalloys 718 Metall. Appl., TMS, 1989: pp.
577 219–228. https://doi.org/10.7449/1989/Superalloys_1989_219_228.
578 [26] H.L. Eiselstein, Metallurgy of a Columbium-Hardened Nickel-Chromium-Iron Alloy, in: Adv.
579 Technol. Stainl. Steels Relat. Alloy., ASTM International, 100 Barr Harbor Drive, PO Box C700,
580 West Conshohocken, PA 19428-2959, 1965: pp. 62-62–18. https://doi.org/10.1520/STP43733S.
581 [27] M.C. Chaturvedi, Y. Han, Strengthening mechanisms in Inconel 718 superalloy, Met. Sci. 17
582 (1983) 145–149. https://doi.org/10.1179/030634583790421032.
583 [28] M. Sundararaman, P. Mukhopadhyay, S. Banerjee, Precipitation of the δ-Ni3Nb phase in two
584 nickel base superalloys, Metall. Trans. A. 19 (1988) 453–465.
585 https://doi.org/10.1007/BF02649259.
586 [29] M. Sundararaman, P. Mukhopadhyay, S. Banerjee, Some aspects of the precipitation of metastable
587 intermetallic phases in INCONEL 718, Metall. Trans. A. 23 (1992) 2015–2028.

https://doi.org/10.1007/BF02647549.

[30] M. Wang, M. Song, G.S. Was, J.L. Nelson, The roles of thermal mechanical treatment and δ phase in the stress corrosion cracking of alloy 718 in primary water, Corros. Sci. 160 (2019) 108168. https://doi.org/10.1016/j.corsci.2019.108168.

[31] S. Mahadevan, S. Nalawade, J.B. Singh, A. Verma, B. Paul, K. Ramaswamy, Evolution of δ phase microstructure in alloy 718, 7th Int. Symp. Superalloy 718 Deriv. 2010. 2 (2010) 737–750. https://doi.org/10.1002/9781118495223.ch57.

[32] C. Silva, M. Song, K. Leonard, M. Wang, G. Was, J. Busby, Characterization of alloy 718 subjected to different thermomechanical treatments, Mater. Sci. Eng. A. 691 (2017) 195–202. https://doi.org/10.1016/j.msea.2017.03.045.

[33] Standard Specification for Precipitation-Hardening Nickel Alloy (UNS N07718) Plate , Sheet , and Strip for High-Temperature Service, Annu. B. ASTM Stand. 07 (2010) 7–10. https://doi.org/10.1520/B0670-07.

[34] M.N. Gussev, R.H. Howard, K.A. Terrani, K.G. Field, Sub-size tensile specimen design for in-reactor irradiation and post-irradiation testing, Nucl. Eng. Des. 320 (2017) 298–308. https://doi.org/10.1016/j.nucengdes.2017.06.008.

[35] M.N. Gussev, J.T. Busby, K.G. Field, M.A. Sokolov, S.E. Gray, Role of scale factor during tensile testing of small specimens, ASTM Spec. Tech. Publ. STP 1576 (2015) 31–49. https://doi.org/10.1520/STP157620140013.

[36] S. Taller, T. Austin, V. Paquit, K. Terrani, Report on Properties and Microstructure of 3D Printed Inc-718, ORNL/TM-2021/2149, Oak Ridge, TN (United States), 2021. https://doi.org/10.2172/1820785.

[37] S. Specification, B670: Standard Specification for Precipitation-Hardening Nickel Alloy (UNS N07718) Plate , Sheet, and Strip for High-Temperature Service, Annu. B. ASTM Stand. 07 (2010) 7–10. https://doi.org/10.1520/B0670-07R18.2.

[38] C. Kumara, A.R. Balachandramurthi, S. Goel, F. Hanning, J. Moverare, Toward a better

understanding of phase transformations in additive manufacturing of Alloy 718, Materialia. 13 (2020) 100862. https://doi.org/10.1016/j.mtla.2020.100862.

[39] A.K. Sahu, S. Bag, Design of a double aging treatment for the improvement of mechanical and microstructural properties of pulse micro-plasma arc welded alloy 718, J. Mater. Sci. 56 (2021) 13400–13415. https://doi.org/10.1007/s10853-021-06121-8.

[40] F. Bachmann, R. Hielscher, H. Schaeben, Texture analysis with MTEX- Free and open source software toolbox, Solid State Phenom. 160 (2010) 63–68. https://doi.org/10.4028/www.scientific.net/SSP.160.63.

[41] G. Cliff, G.W. Lorimer, The quantitative analysis of thin specimens, J. Microsc. 103 (1975) 203–207. https://doi.org/10.1111/j.1365-2818.1975.tb03895.x.

[42] S. Taller, L. Scime, K. Terrani, Utilizing a Dynamic Segmentation Convolutional Neural Network for Microstructure Analysis of Additively Manufactured Superalloy 718, Microsc. Microanal. 27 (2021) 3110–3112. https://doi.org/10.1017/s143192762101076x.

[43] J. Schindelin, I. Arganda-Carreras, E. Frise, V. Kaynig, M. Longair, T. Pietzsch, S. Preibisch, C. Rueden, S. Saalfeld, B. Schmid, J.Y. Tinevez, D.J. White, V. Hartenstein, K. Eliceiri, P. Tomancak, A. Cardona, Fiji: An open-source platform for biological-image analysis, Nat. Methods. 9 (2012) 676–682. https://doi.org/10.1038/nmeth.2019.

[44] K. Yuan, W. Guo, P. Li, Y. Zhang, X. Li, X. Lin, Thermomechanical behavior of laser metal deposited Inconel 718 superalloy over a wide range of temperature and strain rate: Testing and constitutive modeling, Mech. Mater. 135 (2019) 13–25. https://doi.org/10.1016/j.mechmat.2019.04.024.

[45] A. Oradei-Basile, J.F. Radavich, A Current T-T-T Diagram for Wrought Alloy 718, (2012) 325–335. https://doi.org/10.7449/1991/superalloys_1991_325_335.

[46] J.F. Radavich, The Physical Metallurgy of Cast and Wrought Alloy 718, in: Superalloys 718 Metall. Appl., TMS, 2004: pp. 229–240. https://doi.org/10.7449/1989/Superalloys_1989_229_240.

[47] A. Segerstark, J. Andersson, L.E. Svensson, O. Ojo, Microstructural characterization of laser metal powder deposited Alloy 718, Mater. Charact. 142 (2018) 550–559. https://doi.org/10.1016/j.matchar.2018.06.020.

[48] G.F. Knoll, Radiation Detection and Measurement, 3rd Editio, John Wiley & Sons, Inc., 2000.

[49] S.G.K. Manikandan, D. Sivakumar, M. Kamaraj, Physical metallurgy of alloy 718, Weld. Inconel 718 Superalloy. (2019) 1–19. https://doi.org/10.1016/b978-0-12-818182-9.00001-3.

[50] D.D. Keiser, H.L. Brown, Review of the physical metallurgy of Alloy 718, U.S. Department of Energy, 1976. https://doi.org/10.2172/4016087.

[51] T.S. Byun, K. Farrell, Tensile properties of Inconel 718 after low temperature neutron irradiation, J. Nucl. Mater. 318 (2003) 292–299. https://doi.org/10.1016/S0022-3115(03)00006-0.

[52] H.M. Ledbetter, R.P. Reed, Elastic Properties of Metals and Alloys, I. Iron, Nickel, and Iron-Nickel Alloys, J. Phys. Chem. Ref. Data. 2 (1973) 531–618. https://doi.org/10.1063/1.3253127.

[53] S. Umekawa, On Young's Moduli of Nickel-Copper and Nickel-Cobalt Alloys, J. Japan Inst. Met. 18 (1954) 387–390. https://doi.org/10.2320/jinstmet1952.18.7_387.

[54] Y. Shirakawa, K. Numakura, Elasticity Constants of Single Crystals of Nickel-Copper Alloys, Sci. Reports Res. Institutes, Tohoku Univ. Ser. A, Physics, Chem. Metall. 10 (1958) 51–57. http://hdl.handle.net/10097/26859.

[55] Y. Shirakawa, K. Numakura, On Young's Modulus and Grain Size in Nickel-Copper Alloys, Sci. Reports Res. Institutes, Tohoku Univ. Ser. A, Physics, Chem. Metall. 10 (1958) 110–119. http://hdl.handle.net/10097/26866.

[56] Y. Shirakawa, Y. Tanji, H. Moriya, I. Oguma, The Elastic Constants of Ni and Ni-Fe (fcc) Alloys, Sci. Reports Res. Institutes, Tohoku Univ. Ser. A, Physics, Chem. Metall. 21 (1969) 187–200. http://hdl.handle.net/10097/27496.

[57] M. Yamamoto, On Elastic Constants of Nickel Crystals, Phys. Rev. 77 (1950) 566–566. https://doi.org/10.1103/PhysRev.77.566.

[58] H. Masumoto, H. Saito, S. Sawaya, Thermal Expansion and Temperature Dependence of Young's Modulus of Nickel-Copper Alloys, Trans. Japanese Inst. Met. 11 (1970).

[59] S. Li, Y. Wang, X. Wang, F. Xue, G-phase precipitation in duplex stainless steels after long-term thermal aging: A high-resolution transmission electron microscopy study, J. Nucl. Mater. 452 (2014) 382–388. https://doi.org/10.1016/j.jnucmat.2014.05.069.

[60] Y. Matsukawa, T. Takeuchi, Y. Kakubo, T. Suzudo, H. Watanabe, H. Abe, T. Toyama, Y. Nagai, The two-step nucleation of G-phase in ferrite, Acta Mater. 116 (2016) 104–113. https://doi.org/10.1016/j.actamat.2016.06.013.

[61] Y. Fan, T.G. Liu, L. Xin, Y.M. Han, Y.H. Lu, T. Shoji, Thermal aging behaviors of duplex stainless steels used in nuclear power plant: A review, J. Nucl. Mater. (2020) 152693. https://doi.org/10.1016/j.jnucmat.2020.152693.

[62] P.B. Hirsch, F.J. Humphreys, Plastic deformation of two-phase alloys containing small nondeformable particles, in: A.S. Argon (Ed.), Phys. Strength Plast., M. I. T. Press, 1969: p. 189.

[63] F.R.N. Nabarro, Fifty-year study of the Peierls-Nabarro stress, Mater. Sci. Eng. A. 234–236 (1997) 67–76. https://doi.org/10.1016/s0921-5093(97)00184-6.

[64] R.E. Stoller, S.J. Zinkle, On the relationship between uniaxial yield strength and resolved shear stress in polycrystalline materials, J. Nucl. Mater. 283–287 (2000) 349–352. https://doi.org/10.1016/S0022-3115(00)00378-0.

[65] L. Tan, J.T. Busby, Formulating the strength factor α for improved predictability of radiation hardening, J. Nucl. Mater. 465 (2015) 724–730. https://doi.org/10.1016/j.jnucmat.2015.07.009.

[66] G.E. Lucas, The evolution of mechanical property change in irradiated austenitic stainless steels, J. Nucl. Mater. 206 (1993) 287–305. https://doi.org/10.1016/0022-3115(93)90129-M.

[67] B.L. Eyre, Transmission electron microscope studies of point defect clusters in fcc and bcc metals, J. Phys. F Met. Phys. 3 (1973) 422–470. https://doi.org/10.1088/0305-4608/3/2/009.

[68] D. Hull, D.J. Bacon, Strength of Crystalline Solids, Introd. to Dislocations. 1 (2011) 205–249. https://doi.org/10.1016/b978-0-08-096672-4.00010-4.

[69] V. Bata, E. V. Pereloma, An alternative physical explanation of the Hall-Petch relation, Acta Mater. 52 (2004) 657–665. https://doi.org/10.1016/j.actamat.2003.10.002.

[70] J.A. Turner, J. Belak, N. Barton, M. Bement, N. Carlson, R. Carson, S. DeWitt, J.L. Fattebert, N. Hodge, Z. Jibben, W. King, L. Levine, C. Newman, A. Plotkowski, B. Radhakrishnan, S.T. Reeve, M. Rolchigo, A. Sabau, S. Slattery, B. Stump, ExaAM: Metal additive manufacturing simulation at the fidelity of the microstructure, Int. J. High Perform. Comput. Appl. 36 (2022) 13–39. https://doi.org/10.1177/10943420211042558.

[71] A.S. Agazhanov, D.A. Samoshkin, Y.M. Kozlovskii, Thermophysical properties of Inconel 718 alloy, J. Phys. Conf. Ser. 1382 (2019). https://doi.org/10.1088/1742-6596/1382/1/012175.

[72] D. Hull, D.J. Bacon, Elastic Properties of Dislocations, Introd. to Dislocations. (2011) 63–83. https://doi.org/10.1016/b978-0-08-096672-4.00004-9.

[73] A.A. Kohnert, L. Capolungo, A novel approach to quantifying the kinetics of point defect absorption at dislocations, J. Mech. Phys. Solids. 122 (2019) 98–115. https://doi.org/10.1016/j.jmps.2018.08.023.

[74] A.A. Kohnert, L. Capolungo, Spectral discrete dislocation dynamics with anisotropic short range interactions, Comput. Mater. Sci. 189 (2021) 110243. https://doi.org/10.1016/j.commatsci.2020.110243.

Appendix

A.1 Engineering Stress-Strain Curves for All Specimens in this Study

While averages and representative values capture the overall behavior of the material, transparency requires that all necessary information be included. Therefore, the stress-strain curves for each tensile test are provided here in Figures Figure A.14 – Figure A.17.

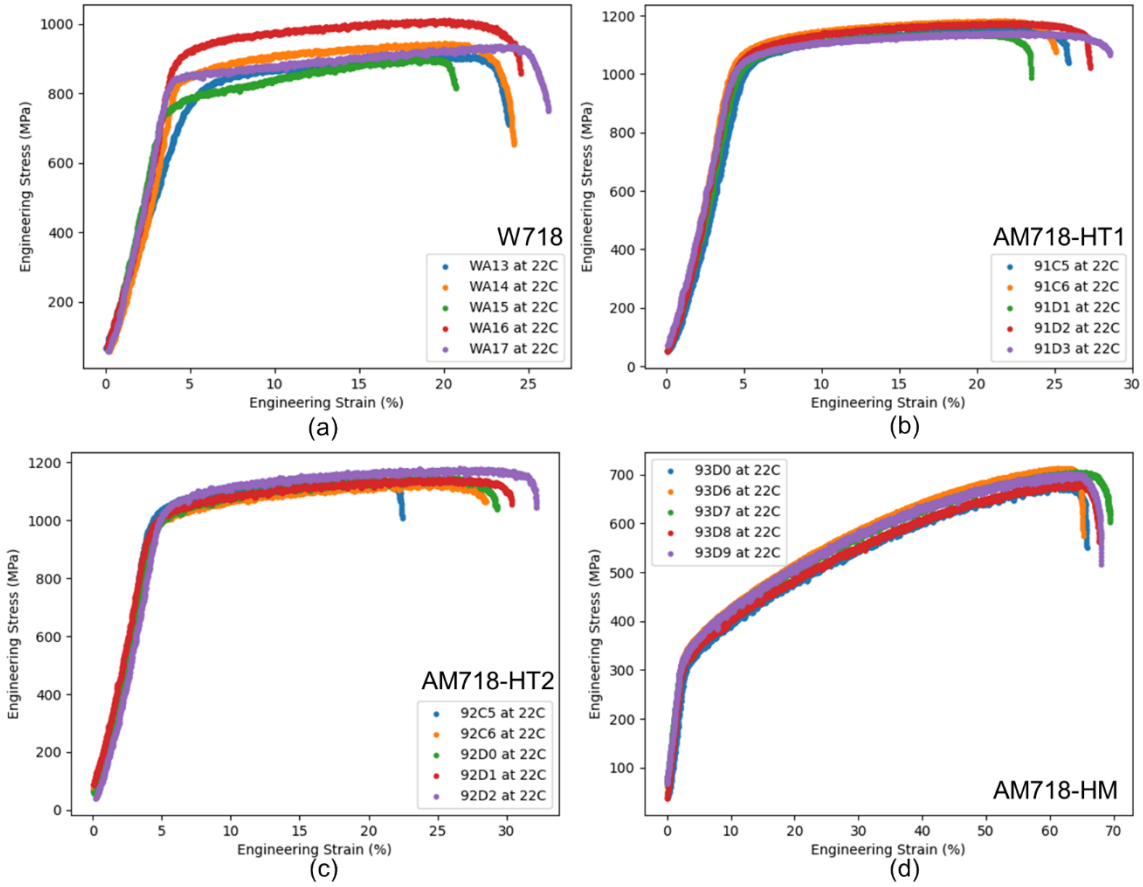

Figure A.14. Individual engineering stress-strain curves for wrought superalloy 718 (a) and heat-treated AM superalloy 718 (b–d) at room temperature.

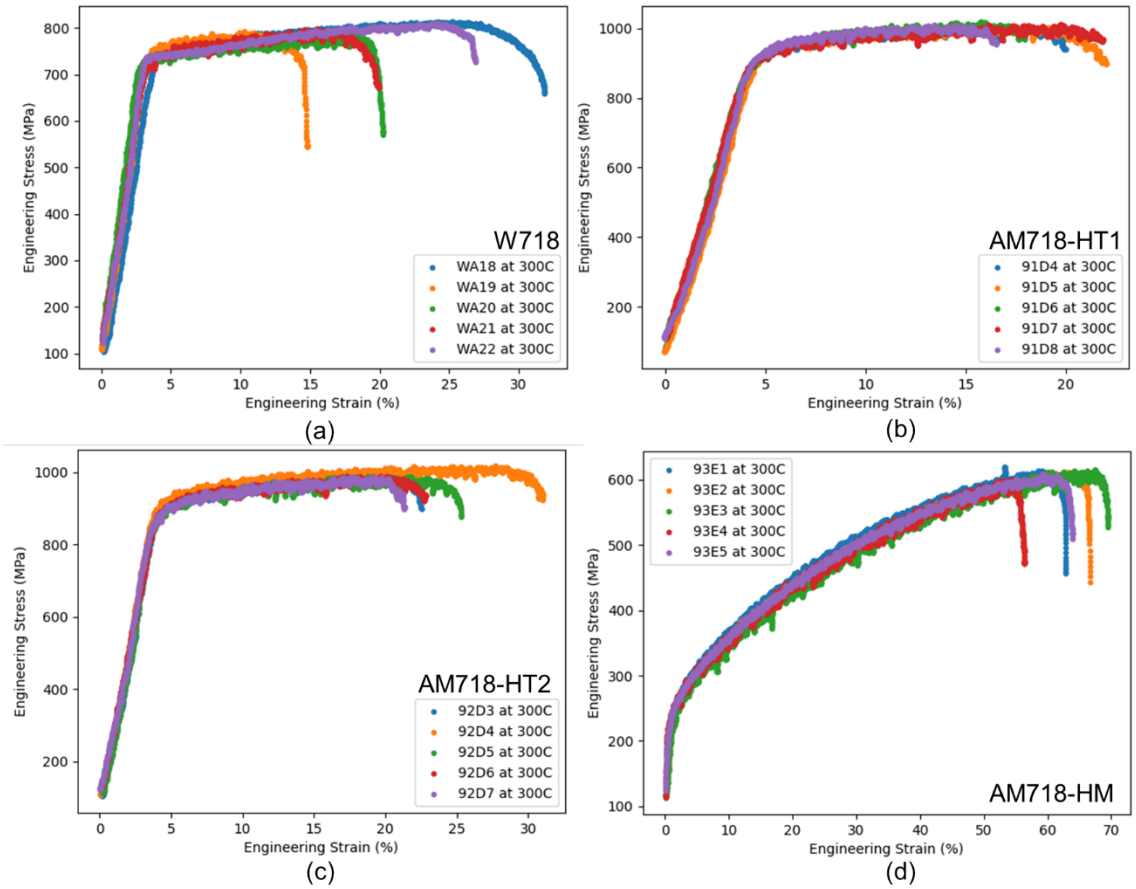

719

720 **Figure A.15. Individual engineering stress-strain curves for wrought superalloy 718 (a) and heat-treated AM superalloy**

721 **718 (b–d) at 300 °C.**

722

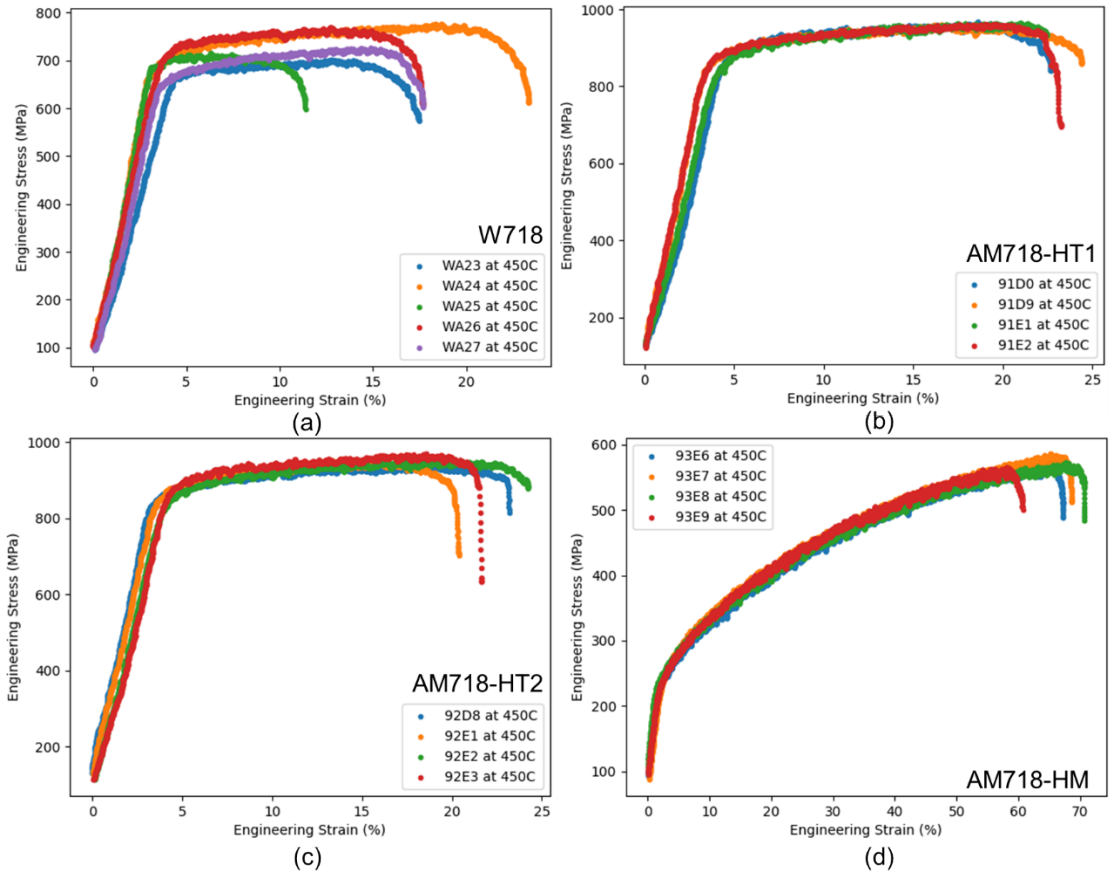

723

724 **Figure A.16. Individual engineering stress-strain curves for wrought superalloy 718 (a) and heat-treated AM superalloy**

725 **718 (b–d) at 450 °C.**

726

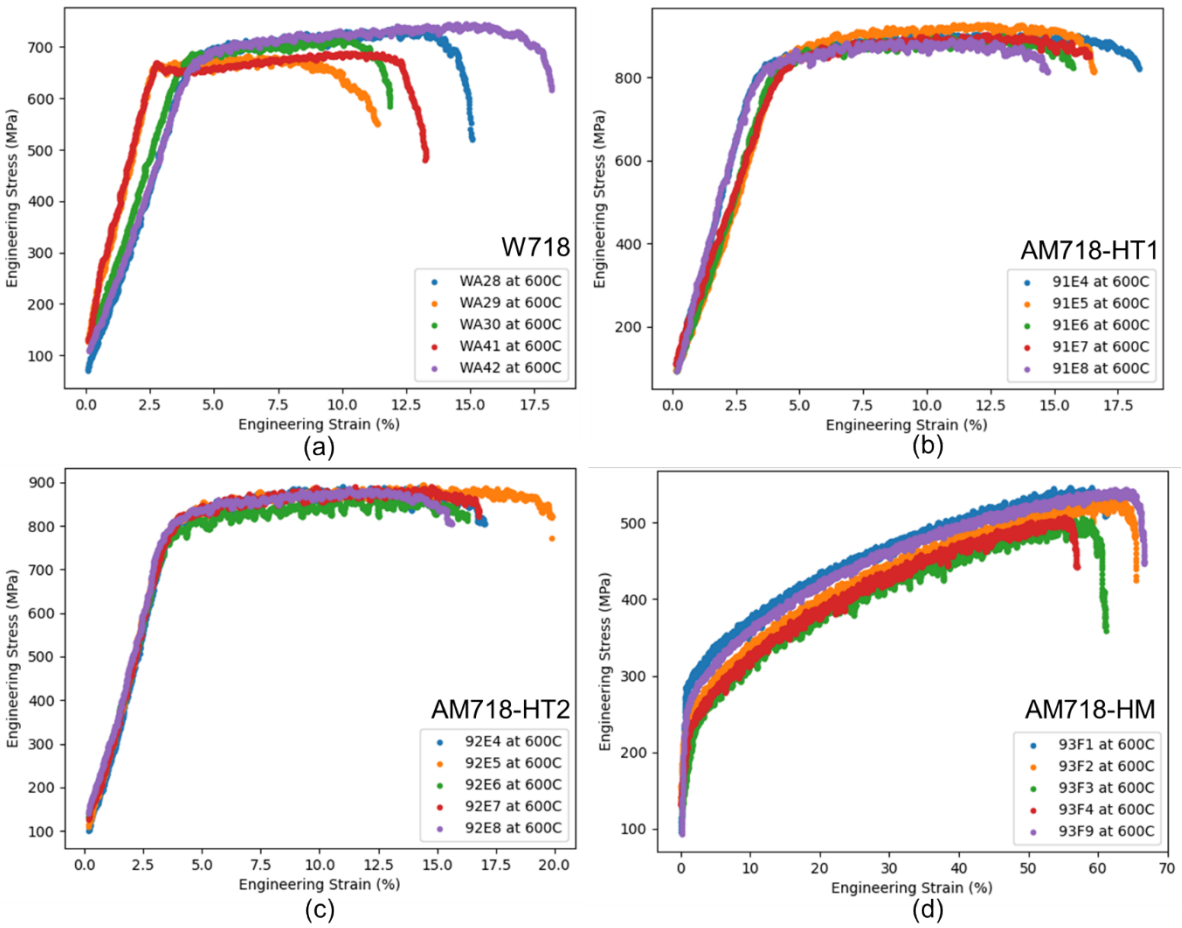

Figure A.17. Individual engineering stress-strain curves for wrought superalloy 718 (a) and heat-treated AM superalloy 718 (b–d) at 600 °C.

A.2 On the Differences in Microstructure in W718 and AM-HT2 for the Same Heat Treatments

In an ideal scenario, putting two samples of the same material in the same furnace for heat treatment and subjecting them to the same temperature history would result in the same microstructure and properties. In this study, both AM718-HT2 and W718 went through the same heat treatment history, but they resulted in different microstructures and properties. The AM718 block was homogenized and aged in the form of a block with dimensions of 15 × 30 × 60 mm for its length, width, and height respectively. The W718 was heat treated as a cylinder with a diameter of 25.4 mm and a height of 22 mm. The furnace used was an open-air furnace, so the method of heat transfer to the samples was natural convection. Thus, the Biot

number can be used as an indication of the thermal resistance inside of each body and at the surface of each body:

$$Bi = \frac{\bar{h}}{k}\left(\frac{V}{A}\right), \tag{A.4}$$

where $\bar{h}$ is the average convective heat transfer coefficient for air, k is the thermal conductivity of alloy 718, V is the volume of the component, and A is the surface area available for heat transfer. Using the properties of 718 from Agazhanov et al. [71] and the dimensions noted above, the Biot number for each block is 0.0071, and for the W718 cylinder, the Biot number is 0.0067. The absolute values of both are small (<0.1), implying that heat conduction inside 718 is much faster than heating from the environment, so there are negligible temperature gradients inside each piece. Because of this low Biot number, the transient temperature of each piece can be estimated using the lumped capacitance model of heat transfer, as shown in Eq. A.5:

$$\frac{T(t) - T_\infty}{T_i - T_\infty} = e^{-t\frac{A\bar{h}}{\rho c V}}, \tag{A.5}$$

where $T(t)$ is the temperature of the metal at time t, T_∞ is the temperature of the heat reservoir, T_i is the initial temperature of the piece, and c is the specific heat capacity. The time-dependent temperature of each piece is shown in Figure A.18 and is solved with time- and temperature-dependent material properties updating every 1 second based on the average temperature of the previous three timesteps. From this estimation, the cylinder heats up quicker than the block, resulting in a difference in the time at which each piece reaches the same temperature. During heat treatment, the aging time was started when a thermocouple on the surface of the AM718 block read within 10 °C of the target temperature, which is designated as T_{10} in Figure A.18. When the AM718 block reaches T_{10}, the cylinder of W718 has already been at the aging temperature for about 1.5 hours. Based on the T-T-T diagram [45], for an aging temperature of 718 °C, W718 would be closer to the boundary at which delta phase forms. Thus, while the same heat treatments and aging were used on AM718 and W718, the sample geometry in the furnace led to an over-aging of the W718 and significant formation of intragranular delta phase precipitates.

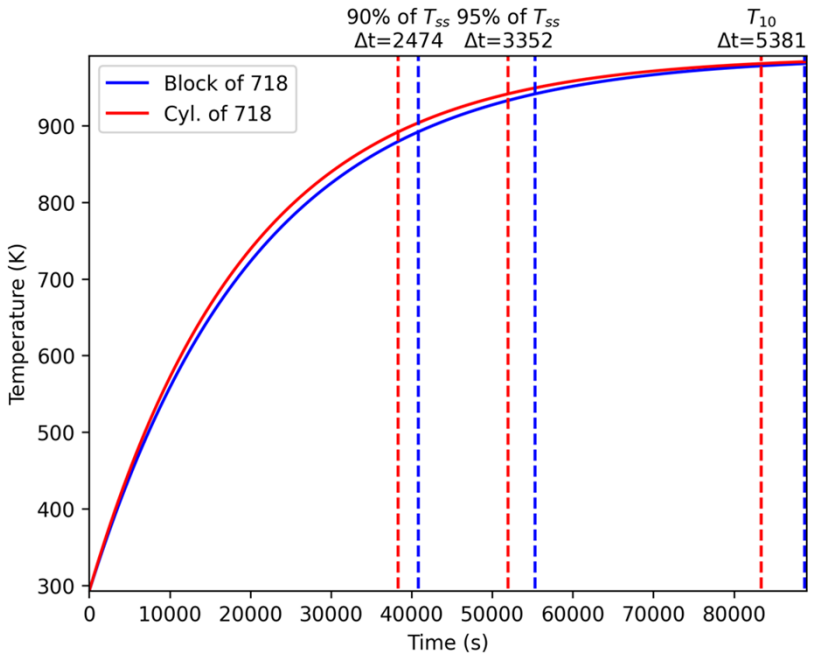

762

763 **Figure A.18. Transient temperature build-up in superalloy 718 blocks and cylinder through the lumped capacitance**
764 **method.**

765 ### A.3 On the Use of Theoretical Strength Factors

766 In the work presented in the main manuscript, no assumptions were made in the strength
767 coefficients. Traditionally, the strengthening coefficients, α, are usually adjusted to obtain a best fit when
768 compared with experimental data. This approach limits any predictability of the model and neglects any
769 contributions of precipitate shape or size. The effects of the precipitate shape and size on the strength factor
770 were considered by Tan and Busby [65] in a paper which presented forms for α for spherical, rod-shaped,
771 and thin plate precipitates. In this study, the γ' precipitates were observed as spherical features, whereas the
772 γ" and intragranular δ precipitates were found as thin disk or plate precipitates. Thus, the relevant
773 strengthening coefficients from Tan and Busby are as follows:

774 $$\text{Spherical } \alpha_{SP} = \frac{0.135}{(1-\boldsymbol{\nu})^{1/2}(1-0.816\boldsymbol{d}\sqrt{\boldsymbol{Nd}})} ln\left(\frac{0.816\boldsymbol{d}}{r_0}\right). \quad \text{(A.6)}$$

775 $$\text{Thin-plate } \alpha_{PP} = \frac{0.271\boldsymbol{A}}{(1-\nu)^{1/2}\sqrt{\boldsymbol{ND}}(16-\pi\boldsymbol{tA})} ln\left(\frac{0.637\boldsymbol{D}}{r_0}\right), \text{ with } A = \sqrt{16\pi\boldsymbol{ND}+4\boldsymbol{ND}^2-\pi^2\boldsymbol{NDt}}, \quad \text{(A.7)}$$

where N is the number density of the precipitating phase, d is the average diameter of spherical precipitates, D is the large diameter of thin plate precipitates, t is the thickness of the thin plate precipitate, ν is Poisson's ratio (~0.3), and r_0 is the dislocation core radius (r_0~**b** to 4**b** [72]). A value of r_0=4**b** was chosen for estimating the dislocation core radius, whereas all other values were calculated from the characterized microstructures. Lucas [66] summarizes the reported values of different types of defects and categorizes them into three groups: (1) weak barriers such as small bubbles/loops and dislocations with $\alpha < 0.25$, (2) intermediate barriers such as Frank loops and small precipitates with $0.33 < \alpha < 0.45$, and (3) strong barriers such as voids and large precipitates with α~1 obstacles. The estimations of α for γ', γ'', and δ precipitates are included in Table A.7, along with their contributions to the yield strength calculated using Eq. (3) and the microstructure presented in Table 4. This approach resulted in strength coefficients suggesting that each phase is still in the weak-to-intermediate barrier range. However, with these strength coefficients, the summation of contributions from each phase exceeds the measured yield stresses at each tensile test temperature, suggesting that these strength coefficients overestimate the strength of the barriers. Considering the precipitate-dislocation interaction, before the dislocation core becomes pinned on the precipitate, the precipitate and dislocation will first interact through the strain fields around them. Although the size of the strain field is not directly known, the works of Kohnert and Capolungo suggest that the strain field around a dislocation can be as large as 10**b** [73,74]. If this strain field (r_0~10**b**) is used instead of the dislocation core radius, then the strengthening coefficients decrease, and the precipitates become barrier strengths similar to those determined through solving the linear least squares problem as done in the main manuscript shown in Table 6.

Table A.7. Coefficients determined through a theoretical approach to correlate microstructure to yield strength with estimated contributions from γ', γ'', and δ phase precipitates.

Property	Tensile test temperature (°C)	W718	AM718-HT1	AM718-HT2
$\alpha_{\gamma'}$ (unitless), r_0~4**b**	N.A.	0.193	0.257	0.228
$\alpha_{\gamma''}$ (unitless), r_0~4**b**	N.A.	0.250	0.328	0.306

α_δ (unitless), r_0~4**b**	N.A.	0.237	0.288	0.256
σ_{yield} (MPa)	22	873 ± 131	1214 ± 15.6	1125 ± 38.2
$\Delta\sigma_{\gamma'}$ (MPa)	22	148.75	238.76	291.96
$\Delta\sigma_{\gamma''}$ (MPa)	22	780.92	1314.68	1317.68
$\Delta\sigma_\delta$ (MPa)	22	478.61	293.75	208.87
σ_{yield} (MPa)	300	818 ± 32.9	969 ± 78.2	980 ± 26.1
$\Delta\sigma_{\gamma'}$ (MPa)	300	137.44	220.61	269.78
$\Delta\sigma_{\gamma''}$ (MPa)	300	721.58	1214.79	1217.56
$\Delta\sigma_\delta$ (MPa)	300	442.25	271.43	193.00
σ_{yield} (MPa)	450	766 ± 16.1	961 ± 61.5	949±52.3
$\Delta\sigma_{\gamma'}$ (MPa)	450	131.34	210.83	257.81
$\Delta\sigma_{\gamma''}$ (MPa)	450	689.57	1160.89	1163.54
$\Delta\sigma_\delta$ (MPa)	450	422.62	259.39	184.43
σ_{yield} (MPa)	600	751 ± 15.5	931 ± 19.6	907 ± 38.0
$\Delta\sigma_{\gamma'}$ (MPa)	600	125.24	201.04	245.84
$\Delta\sigma_{\gamma''}$ (MPa)	600	657.55	1106.99	1109.51
$\Delta\sigma_\delta$ (MPa)	600	403.00	247.34	175.87
$\alpha_{\gamma'}$ (unitless), r_0~10**b**	N.A.	0.042	0.105	0.075
$\alpha_{\gamma''}$ (unitless), r_0~10**b**	N.A.	0.102	0.173	0.149
α_δ (unitless), r_0~10**b**	N.A.	0.094	0.149	0.119

798